

## ASSESSMENT OF THE PROJECTION-INDUCED POLARIMETRY TECHNIQUE FOR CONSTRAINING THE FOREGROUND SPECTRUM IN GLOBAL 21 CM COSMOLOGY

BANG D. NHAN<sup>1,2,3,7</sup>, DAVID D. BORDENAVE<sup>1,2,7</sup>, RICHARD F. BRADLEY<sup>1,2,4</sup>, JACK O. BURNS<sup>3</sup>,  
KEITH TAUSCHER<sup>3,5</sup>, DAVID RAPETTI<sup>3,6</sup>, AND PATRICIA J. KLIMA<sup>2</sup>

(Dated: August 6, 2019)  
Draft version August 6, 2019

### ABSTRACT

Detecting the cosmological sky-averaged (global) 21 cm signal as a function of observed frequency will provide a powerful tool to study the ionization and thermal history of the intergalactic medium (IGM) in the early Universe ( $\sim 400$  million years after the Big Bang). The greatest challenge in conventional total-power global 21 cm experiments is the removal of the foreground synchrotron emission ( $\sim 10^3\text{-}10^4$  K) to uncover the weak cosmological signal (tens to hundreds of mK), especially since the intrinsic smoothness of the foreground spectrum is corrupted by instrumental effects. Although the EDGES team has recently reported an absorption profile at 78 MHz in the sky-averaged spectrum, it is necessary to confirm this detection with an independent approach. The projection effect from observing anisotropic foreground source emission with a wide-view antenna pointing at the North Celestial Pole (NCP) can induce a net polarization, referred as the Projection-Induced Polarization Effect (PIPE). Due to Earth's rotation, observation centered at the circumpolar region will impose a dynamic sky modulation on the net polarization's waveforms which is unique to the foreground component. In this study, we review the implementation practicality and underlying instrumental effects of this new polarimetry-based technique with detailed numerical simulation and a testbed instrument, the Cosmic Twilight Polarimeter (CTP). In addition, we explore an SVD-based analysis approach for separating the foreground and instrumental effects from the background global 21 cm signal using the sky-modulated PIPE.

*Subject headings:* dark ages, reionization, first stars - techniques: polarimetric - methods: observational

### 1. INTRODUCTION

Measuring the redshifted 21 cm line corresponding to the hyperfine transition of neutral hydrogen (HI) has been considered the primary means to probe the thermal and ionization history of the intergalactic medium (IGM) in the high-redshift Universe, during the three main phases known as: the Dark Ages ( $1,100 \gtrsim z \gtrsim 30$ ), Cosmic Dawn ( $30 \gtrsim z \gtrsim 15$ ), and the Epoch of Reionization (EoR,  $15 \gtrsim z \gtrsim 6$ ) (e.g., Furlanetto et al. 2006; Furlanetto 2006; Pritchard & Loeb 2010, 2012; Liu et al. 2013; Barkana 2016). Development of large interferometric arrays has been focusing on measuring the power spectrum of spatial fluctuations in the 21 cm brightness temperature at the end of EoR (e.g., Parsons et al. 2010; Tingay et al. 2013; Bowman et al. 2013; van Haarlem et al. 2013; Paciga et al. 2013; Mellema et al. 2013; DeBoer et al. 2017). At lower frequencies, observations to constrain the limits on the Cosmic Dawn using the 21 cm power spectrum have been attempted by the Low-Frequency Array's Low Band Antenna (LOFAR-LBA,

Gehlot et al. 2018).

Meanwhile, for the last decade or so, there have also been efforts to search for the sky-averaged monopole component of the redshifted 21 cm signal by using single dipole antennas or compact arrays consisting of a small number of antenna elements over a large frequency range ( $\sim 50 \leq \nu \leq 200$  MHz). Some of the current and past sky-averaged (global) 21 cm experiments include: the Experiment to Detect the Global EoR Signature (EDGES I & II, Bowman et al. 2008; Bowman & Rogers 2010; Monsalve et al. 2017), the Shaped Antenna Measurement of the Background Radio Spectrum (SARAS 1 & 2, Patra et al. 2013; Singh et al. 2017), the Broadband Instrument for Global Hydrogen Reionization Signal (BIGHORNS, Sokolowski et al. 2015a), the Large-Aperture Experiment to Detect the Dark Ages (LEDA, Greenhill & LEDA Collaboration 2015; Price et al. 2018), the Sonda Cosmológica de las Islas para la Detección de Hidrógeno Neutro (SCI-HI, Voytek et al. 2014), and the Probing Radio Intensity at high- $z$  from Marion (PRIZM, Philip et al. 2019).

Theoretical studies have shown that global measurement of the 21 cm signal can complement the power spectrum measurements by providing meaningful physical parameters for the evolution of the IGM (e.g., Furlanetto 2006; Pritchard & Loeb 2012; Liu et al. 2013; Mirocha et al. 2013, 2015, 2017). These global experiments are designed to measure the total power of the sky signal, including both the redshifted 21 cm background and the foreground synchrotron emission originated from both Galactic and extragalactic sources.

Among the measurement and systematic errors, the

<sup>1</sup> Department of Astronomy, University of Virginia, Charlottesville, VA 22903, USA bnhan@nrao.edu

<sup>2</sup> National Radio Astronomy Observatory (NRAO) Technology Center (NTC), Charlottesville, VA 22903, USA

<sup>3</sup> Center for Astrophysics and Space Astronomy (CASA), Department of Astrophysical and Planetary Sciences, University of Colorado, Boulder, CO 80309, USA

<sup>4</sup> Department of Electrical and Computer Engineering, University of Virginia, Charlottesville, VA 22903, USA

<sup>5</sup> Department of Physics, University of Colorado, Boulder, CO 80309, USA

<sup>6</sup> NASA Ames Research Center, Moffett Field, CA 94035, USA

<sup>7</sup> NRAO Grote Reber Doctoral Research Fellow at NTC

foreground emission is the strongest contaminant since it is at least four orders of magnitude ( $\sim 10^3$ - $10^4$  K) stronger than the cosmological 21 cm background (tens to hundreds of mK). Nonetheless, the foreground spectrum is smooth and lacks significant spectral structures (Shaver et al. 1999; Tegmark et al. 2000; Petrovic & Oh 2011; Kogut 2012), whereas the global 21 cm signal is expected to vary on the scale of tens of MHz. Motivated by its spectral smoothness, the foreground spectrum is typically approximated by a polynomial function to separate it from the global 21 cm features. For example, one common parametrization is the log-log polynomial between the brightness temperature and frequency (Pritchard & Loeb 2010; Bowman & Rogers 2010; Harker et al. 2012),

$$\log \hat{T}_{fg}(\nu) = \sum_{n=0}^{m>0} c_n (\log \nu)^n, \quad (1)$$

where  $\hat{T}_{fg}(\nu)$  is the estimated foreground spectrum with polynomial coefficient  $c_n$  of order  $n$  up to a maximum order  $m$ .

In principle, the background global 21 cm signal can then be determined by simultaneously fitting and subtracting the approximated foreground spectrum from the observed spectrum, after calibrating for instrumental effects. However, the order of the fitting polynomial can alter the spectral structures in the residual spectrum. To mitigate this, using a frequency-independent antenna model, Sathyanarayana Rao et al. (2017a) have shown that approximating the foreground spectrum with maximally smooth (MS) polynomials can produce a fit more resilient to the fitting order, and thus preserve the background signal structure better.

Nonetheless, spectral smoothness in the foreground spectrum is highly susceptible to corruptions by frequency-dependent antenna beam patterns (or antenna beam chromaticity) and other instrumental systematics, thus complicating the foreground fitting. Some studies (Bernardi et al. 2015; Mozdzen et al. 2016; Monsalve et al. 2017) have suggested that beam chromaticity is not anticipated to compromise the extraction of the background signal if certain level of beam smoothness can be achieved through special antenna designs and modeling. In practice, obtaining a true frequency-independent beam over a large frequency range can be challenging due to intrinsic characteristics of a broadband antenna. Any uncorrected residual spectral structures from the beam can still bias the recovered cosmological signal.

In recent results from EDGES II, Bowman et al. (2018) have identified an absorption feature centered at about 78 MHz which has the potential to be the cosmological signal. However, there is concern as to whether this feature is a byproduct from fitting errors (Hills et al. 2018) or potential instrumental artifacts such as absorption features induced by a resonant mode excited in the antenna ground plane (Bradley et al. 2019). As this active debate in the community continues, it is imperative to explore a different measurement approach for potential follow-up observations.

In Nhan et al. (2017) (hereinafter NB17), using simulations with an idealized frequency-independent circular Gaussian beam, we demonstrated that the dynamic modulation of foreground emission when pointing the an-

tenna at a celestial pole can imprint unique signatures in the temporal waveforms of the net polarization. This polarization, referred to as the Projection-Induced Polarization Effect (PIPE), is induced by geometrical projection of the anisotropic distribution of foreground sources on the antenna plane when the signal is coupled to the antenna beam. Importantly, since the isotropic cosmological background (spatial fluctuations with angular scale  $< 2^\circ$ , Bittner & Loeb 2011) does not produce a net polarization, NB17 showed that Fourier decomposition of the unique waveforms in the sky-modulated PIPE at each observed frequency helps to reconstruct a copy of the foreground spectrum without invoking any polynomial fit as in the conventional approach.

While a variety of implementation aspects are discussed in NB17, the PIPE simulations there lack realistic instrumental systematics, such as beam chromaticity, environmental effects on beam patterns, and observational effects when observing at a lower latitude other than the geographic poles to achieve foreground modulation on the PIPE. In this study, we extend that framework to more in-depth numerical simulations to further evaluate the proposed technique using semi-realistic antenna beam models acquired from the computational electromagnetic (CEM) simulation software, CST<sup>8</sup>.

In conjunction, a prototype instrument, the Cosmic Twilight Polarimeter (CTP), is presented as a working testbed for implementing the network-theory based calibration scheme and observation strategy for the sky-modulated PIPE. In this study, we also explore the use of a Singular Value Decomposition (SVD) based algorithm to separate the foreground signal and complex instrument systematics from the background 21 cm signal by simultaneously constraining all four PIPE Stokes parameters.

The rest of the paper is organized as follows. In Section 2, we review the general approach of the PIPE and its dynamic modulation using Mueller algebra formulation. Our PIPE simulations, including major instrumental effects from the antenna beam, are presented in Section 3. This is followed by instrumentation details and calibration procedures for the CTP prototype in Section 4, where preliminary observation is also analyzed and compared with simulated data. Additionally, implementation aspects and mitigation strategies are discussed in Section 5. Implications of the sky-modulated PIPE on extracting the global 21 cm signal in the use of SVD, to account for a more realistic observational setting, are examined in Section 6. Finally, we conclude this work in Section 7 by summarizing the lessons learned and near-term plans for further improvements on the CTP instrument and evaluating the PIPE approach.

## 2. PROJECTION-INDUCED POLARIZATION EFFECT

### 2.1. *Mathematical Formalism Revisited*

By considering the incoming broadband radio signal to be quasi-monochromatic, the observed induced polarization at each direction and frequency can be represented by a Stokes vector,  $\mathcal{S}_{\text{obs}}(\theta, \phi, \nu)$ , consisting of four Stokes parameters,  $(I, Q, U, V)_{(\theta, \phi, \nu)}$ . As an extension to the Jones matrix used to characterize the antenna response

<sup>8</sup> Computer Simulation Technology, <https://www.cst.com>

in NB17, in this study the Mueller matrix is adopted to describe the PIPE. The  $4 \times 4$  antenna Mueller matrix,  $\mathbf{M}_{\text{ant}}(\theta, \phi, \nu)$ , describes the coupling of the Stokes vector of an incoming signal source to the antenna response to produce the observed Stokes vector as follows,

$$\mathbf{S}_{\text{obs}}(\theta, \phi, \nu) = \mathbf{M}_{\text{ant}}(\theta, \phi, \nu) \mathbf{S}_{\text{src}}(\theta, \phi, \nu), \quad (2)$$

where  $\mathbf{M}_{\text{ant}}(\theta, \phi, \nu)$  is computed as an outer product of the antenna Jones matrix  $\mathbf{J}_{\text{ant}}(\theta, \phi, \nu)$ . The conversion between the two matrices is summarized in Appendix A.

Since the incoming signal is assumed to be unpolarized, the source Stokes vector reduces to  $\mathbf{S}_{\text{src}}(\theta, \phi, \nu) = (I_{\text{src}}, 0, 0, 0)_{(\theta, \phi, \nu)}$ . The observed Stokes vector contains only contribution of the first column in the Mueller matrix. As a result, the observed data contain polarized components contributed by the antenna beam pattern as  $(I_{\text{src}}, 0, 0, 0)_{(\theta, \phi, \nu)} \rightarrow (I_{\text{obs}}, Q_{\text{obs}}, U_{\text{obs}}, V_{\text{obs}})_{(\theta, \phi, \nu)}$ . In radio interferometry, this is considered as a form of polarization leakage (Sutinjo et al. 2015).

For a sky-averaged measurement, the resulting net induced polarization is a vector sum of the Stokes parameters from all directions. Namely, the observed Stokes parameters are incoming signal spatially weighted by the four Mueller components. These net Stokes parameters, sometimes called Stokes antenna temperatures (Piepmeier et al. 2008), observed at each local sidereal time (LST) and frequency channel are parametrized as,

$$I_{\text{net}}(t_{\text{LST}}, \nu) = \frac{\int_{\Omega} M_{11}(\Omega, \nu) I_{\text{src}}(t_{\text{LST}}, \Omega, \nu) d\Omega}{\int_{\Omega} M_{11}(\Omega, \nu) d\Omega}, \quad (3)$$

$$Q_{\text{net}}(t_{\text{LST}}, \nu) = \frac{\int_{\Omega} M_{21}(\Omega, \nu) I_{\text{src}}(t_{\text{LST}}, \Omega, \nu) d\Omega}{\int_{\Omega} M_{21}(\Omega, \nu) d\Omega}, \quad (4)$$

$$U_{\text{net}}(t_{\text{LST}}, \nu) = \frac{\int_{\Omega} M_{31}(\Omega, \nu) I_{\text{src}}(t_{\text{LST}}, \Omega, \nu) d\Omega}{\int_{\Omega} M_{31}(\Omega, \nu) d\Omega}, \quad (5)$$

$$V_{\text{net}}(t_{\text{LST}}, \nu) = \frac{\int_{\Omega} M_{41}(\Omega, \nu) I_{\text{src}}(t_{\text{LST}}, \Omega, \nu) d\Omega}{\int_{\Omega} M_{41}(\Omega, \nu) d\Omega}, \quad (6)$$

where  $M_{i1}(\Omega, \nu)$  are components of the first column in  $\mathbf{M}_{\text{ant}}(\Omega, \nu)$ , with  $d\Omega = \sin \theta d\theta d\phi$ . It is also worth noting that Equation (3) is analogous to the definition of a beam-weighted antenna temperature,  $T_{\text{ant}}(t_{\text{LST}}, \nu)$ , for sky brightness temperature  $T_{\text{sky}}(t_{\text{LST}}, \Omega, \nu)$  (e.g., Kraus 1986; Wilson et al. 2009),

$$T_{\text{ant}}(t_{\text{LST}}, \nu) = \frac{\int_{\Omega} F(\Omega, \nu) T_{\text{sky}}(t_{\text{LST}}, \Omega, \nu) d\Omega}{\int_{\Omega} F(\Omega, \nu) d\Omega}, \quad (7)$$

since  $M_{11} = F = (F_X + F_Y)/2$  as shown in Equation (A7), where  $F_{X,Y}$  are the antenna beam patterns for  $X$  and  $Y$  polarizations.

## 2.2. Foreground Modulation on the Induced Polarization

For illustration purposes only, the basic rationale of utilizing PIPE modulation as a means to separate the foreground from the background signal is presented with three simple scenarios (left column of Figure 1):

- (a) An artificial foreground with four point sources with identical brightness placed at equal distance from the center of the antenna's field of view (FOV),
- (b) Similar to (a), but with one of the point sources

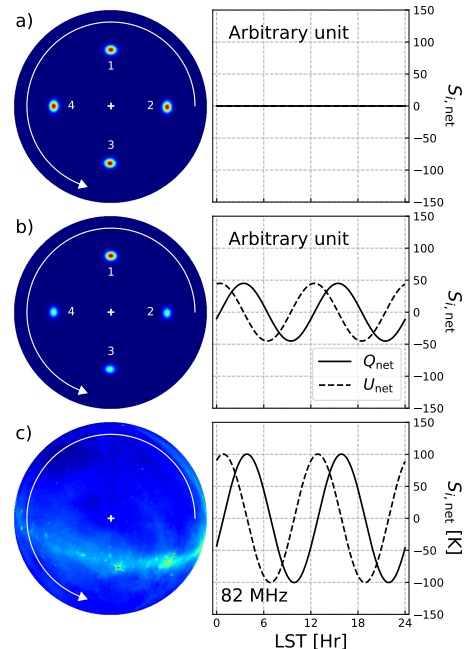


FIG. 1.— Illustrations of three simple scenarios for the PIPE in orthographic projection: (a) Four identical point sources at equal distance from the center (left) produces zero net polarization (right). (b) In a similar situation with four point sources at equal distance, a net polarization is produced when one of the point sources is stronger than the remaining three. (c) As an example at 60 MHz, the anisotropic distribution of foreground emission from the Haslam map centered at the NCP produces a net polarization which can be used to track the foreground, with the signature twice-diurnal periodicity.

(Source #1) brighter than the other three,

- (c) The Haslam full-sky survey map as the sky brightness temperature, scaled from 408 MHz to 60 MHz using a power-law function with a constant spectral index  $\beta = 2.47$ , i.e.,  $T_{\text{sky}}(\nu) = T_{\text{Haslam}}(\nu/408 \text{ MHz})^{-\beta}$ , where  $T_{\text{Haslam}}$  is the Haslam map at 408 MHz.

The complex antenna beams for a pair of simple crossed dipoles above a finite ground plane are obtained from the CST software, to construct  $\mathbf{J}_{\text{ant}}$ . Subsequently, the first column of the corresponding antenna Mueller matrix is computed using Equation (A7) to produce Figure 2. The PIPE for the three scenarios are simulated by computing the beam-weighted mean of the net Stokes parameters for each corresponding foreground maps with Equations (3)-(6).

To dynamically modulate the net polarization, each of the foreground maps is centered at the antenna's bore-sight such that a constant FOV is maintained as the foreground map revolves over 24 sidereal hours. For the first two artificial point-source maps, the FOV is aligned at the circumcenter of the four point sources. For the Haslam map, the antenna pointing is aligned at the North Celestial Pole<sup>9</sup> (NCP), around which the sky revolves.

In scenario (a), due to symmetry in the point source distribution, the equal but opposite two-fold patterns in

<sup>9</sup> Similar effect can be achieved for observing at the South Celestial Pole (SCP) in the Southern Hemisphere.

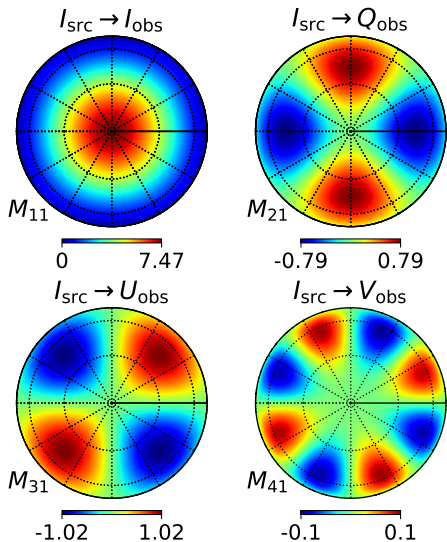


FIG. 2.— Orthographic projection of the first column of the antenna Mueller matrix, computed from the Jones matrix obtained using magnitudes of simulated farfield gain components of a pair of crossed dipoles. The  $M_{11}$  component represents the beam pattern which produces the total intensity of the observed sky region. The  $M_{21}$  and  $M_{31}$  consist of patterns with a two-fold symmetry which respectively contribute to the linear polarizations shown at  $(0^\circ, 90^\circ)$  and  $(+45^\circ, -45^\circ)$ . Meanwhile, the  $M_{41}$ , with a four-fold symmetry, imposes the left-hand and right-hand circular polarizations onto the measurement but at a much lower level relative to the other terms, as indicated in the color bars in linear units. The grid lines are spaced  $30^\circ$  apart in each direction.

$M_{21}$  and  $M_{31}$  (Figure 2) produce a zero net polarization (Figure 1a, right). In the second case, since source #1 is brighter than the others, the source distribution is uneven. Hence, as the sources revolve about the  $M_{21}$  and  $M_{31}$  beams, the amplitude of the  $Q_{\text{net}}(t_{\text{LST}})$  and  $U_{\text{net}}(t_{\text{LST}})$  are modulated by a waveform with an angular frequency of twice the foreground revolution rate (Figure 1b, right).

Similarly, in the last scenario, as asymmetry in the projection of the Haslam map at 60 MHz revolves about the NCP, the amplitude of the resulting net polarization is also modulated by the sky rotation to produce a waveform with a twice-diurnal (two cycles per sidereal day) periodicity, i.e.,  $\omega_{Q,U} = 2\omega_{\text{sky}}$  where  $\omega_{\text{sky}}$  is the sky revolution rate. Also, the phase difference between  $Q_{\text{net}}(t_{\text{LST}})$  and  $U_{\text{net}}(t_{\text{LST}})$  is  $\pi/2$  due to the phase shift between  $M_{21}$  and  $M_{31}$ .

### 2.3. Foreground Removal with the Idealized PIPE

Since the 21 cm background signal has brightness fluctuations on relatively small angular scales compared to the resolvable foreground anisotropy, the 21 cm background is equivalently isotropic in a sky-averaged measurement. Previous sections have illustrated how the PIPE arises solely from projection of the anisotropic foreground source distribution on the antenna plane. By pointing the antenna at the NCP, the modulated waveforms observed in the  $Q_{\text{net}}(t_{\text{LST}}, \nu)$  and  $U_{\text{net}}(t_{\text{LST}}, \nu)$  in principle provide direct means to constrain the foreground component without the confusion of any underlying 21 cm background signal mixed in, unlike the total power spectrum  $I_{\text{net}}(t_{\text{LST}}, \nu)$  which contains both signals.

From the idealized assumptions in NB17, with a spa-

tially constant foreground of spectral index  $\beta$  coupled to a spectrally flat and symmetric Gaussian beam, the simulated PIPE shows that the foreground spectrum  $T_{\text{fg}}(\nu)$  can be reconstructed empirically by Fourier decomposing waveforms of the Stokes  $Q$  or  $U$  at each observed frequency and then compiling magnitudes of the corresponding harmonic modes. The magnitudes of the power spectral density (PSD) for two Stokes waveforms are computed at each harmonic mode  $n$  to construct the Stokes spectra as (Heinzel et al. 2002),

$$S_{S_i, n}^\nu = \frac{(\Delta t)^2}{s_1^2} \left| \sum_{t=1}^M w_{\text{BH4}}(t) S_i(t) e^{-i2\pi t / (nM \Delta t)} \right|^2, \quad (8)$$

where  $S_i$  is one of the four Stokes parameters,  $w_{\text{BH4}}(t)$  is the four-term Blackman-Harris window function to prevent spectral leakage,  $s_1 = \sum_{t=0}^M w_{\text{BH4}}(t)$  is the normalization for discrete data length of  $M$  with an averaging interval  $\Delta t$ .

Hence, in the ideal case, the second harmonic  $S_{Q,2}^\nu$  (or  $S_{U,2}^\nu$ ) corresponding to the two-fold symmetry in  $M_{21}$  (or  $M_{31}$ ) is a scaled version of the foreground spectrum  $T_{\text{fg}}(\nu)$ . The input global 21 cm background model  $\delta T_{\text{b},21\text{cm}}(\nu)$  can then be extracted by iteratively scaling and subtracting the second-harmonic Stokes spectrum from the total sky spectrum  $S_{I,0}^\nu$ , i.e.,  $\delta T_{\text{b},21\text{cm}}(\nu) = T_{\text{sky}}(\nu) - T_{\text{fg}}(\nu) = S_{I,0}^\nu - A S_{Q,2}^\nu$ , where  $A$  is some best-fitted scaling constant. In Section 6, we show that a more sophisticated SVD-based algorithm is needed to constrain the foreground component in the presence of realistic systematics.

## 3. PIPE SIMULATION WITH SEMI-REALISTIC BEAM MODELS

### 3.1. Model Description

Similar to other global 21 cm experiments, the PIPE also requires a broadband and spectrally smooth antenna. Since preliminary analyses suggested that a symmetric beam pattern can improve the sensitivity of sky-modulated PIPE component, a sleeved dipole antenna design with a concentric conductive skirt was adopted for the study. The antenna consists of a pair of orthogonal dual-polarized antenna elements centered between two circular metal plates (or sleeves). The semi-realistic antenna beams used to compute the Mueller matrices across the band were obtained from CST simulation computed with detailed antenna structure model (Figure 3), including a thick ground soil slab beneath the antenna, as well as antenna's ground plane tilting orientation to achieve the foreground modulation effect.

Following a similar framework to that described in the previous section, beam-weighted Stokes parameters for the PIPE were computed using Equations (3)-(6) for the Haslam sky map scaled to the a band of 60-90 MHz using a power-law function with a mean<sup>10</sup> spectral index of  $\beta = 2.47$ .

Additionally, the PIPE simulations in this section also account for obstruction of the Earth's horizon on the FOV of the northern sky centered at the NCP when ob-

<sup>10</sup> The foreground spectral index is known to be distributed between around 2.4 and 2.6 depending on the region in the sky. The effect of a variable  $\beta(\theta, \phi)$  on the PIPE is discussed in Section 5.2.

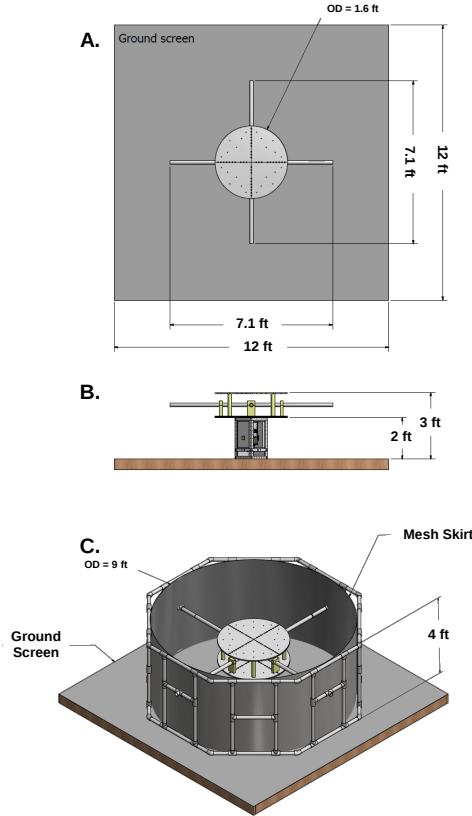


FIG. 3.— 3D model rendering of the sleeved dipole antenna at different views. The conductive cylindrical mesh skirt is for enhancing the beam symmetry between  $E$ - and  $H$ -planes.

serving at lower latitudes. Impacts of the ground soil and horizon obstruction on the induced polarization, presented in Section 3.3 and Section 3.4 respectively, are contrasted to a fiducial model defined in Section 3.2. To decouple these effects from other systematics, the simulations assume an optimal calibration for the electronics, along with the absence of other environmental variables like RFI and ionospheric distortions.

### 3.2. Fiducial Model

The fiducial CST model consists of setting the ground screen of the sleeved dipole parallel to a finite ground soil slab beneath the antenna's ground screen. The fiducial model also assumes that the antenna is located at the Geographic North Pole (GNP) to observe the NCP at the zenith to avoid the Earth's horizon obstruction.

The resulting beams  $F(\theta, \phi, \nu)$  are relatively smooth spatially, with apparent frequency dependence, as shown in the  $E$ -plane ( $\phi = 0^\circ$ ) and  $H$ -plane ( $\phi = 90^\circ$ ) of polarization  $X$  in Figure 4. To further quantify the beam chromaticity of the fiducial beam, we computed the spectral gradients of the beam patterns  $\partial_\nu F(\theta, \phi, \nu)$  evaluated at each fixed  $(\theta, \phi)$ . As shown in Figure 5, the spectral gradients of the  $E$ - and  $H$ -planes plotted side-by-side to their respective beams are showing large gradient variations with  $|\partial_\nu F(\theta, \phi, \nu)| \leq 0.05$  (linear directivity unit per MHz). The significance of these variations is elaborated in Section 5.1.

Without loss of generality, by using this zenith-pointing beam at 82 MHz, the resulting net polarization from the PIPE simulation produces sinusoidal waveforms

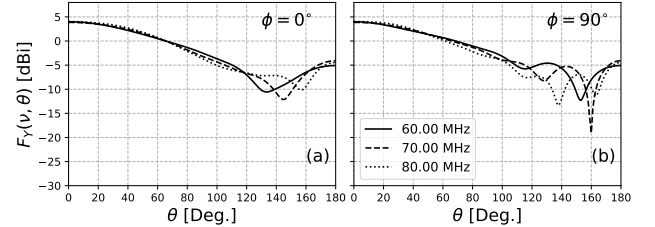


FIG. 4.— Angular plots for the CST beam of the sleeved dipole when the antenna is set parallel to the ground. Hence the  $E$ -plane ( $\phi = 0^\circ$ ) and the  $H$ -plane ( $\phi = 90^\circ$ ) of the beams are smooth and symmetric. The chromaticity is apparent as the beam patterns vary among different frequencies as shown by 60, 70, and 80 MHz.

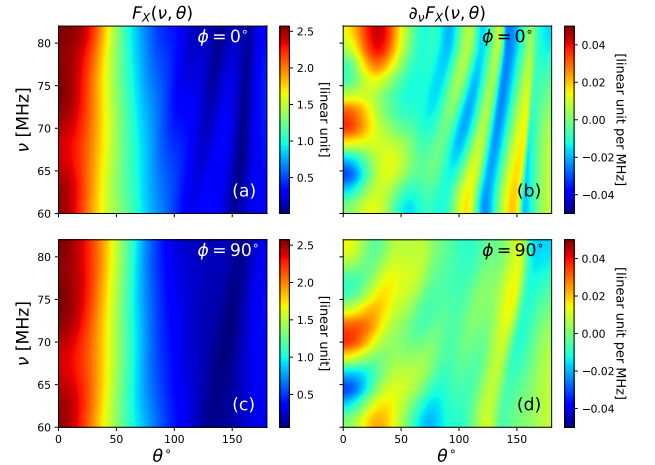


FIG. 5.— (Left) 2D plots of the  $E$ - and  $H$ -planes for the linear directivity in the  $X$ -polarization of the fiducial CST beam model,  $F_X(\theta, \phi, \nu)$ , which has the finite ground screen parallel to the ground soil. (Right) 2D plots of the frequency gradient,  $\partial_\nu F_X(\theta, \phi, \nu)$ , of the beams on the left panels. The strong fringing structures due to interactions between the beam and ground are more apparent in the gradient plots, with  $|\partial_\nu F(\theta, \phi, \nu)| \leq 0.05$  (linear directivity unit per MHz). By symmetry, the beam for  $Y$ -polarization,  $F_Y(\theta, \phi, \nu)$ , shares similar patterns and frequency structures.

with twice-diurnal period in Stokes  $Q_{\text{cal}}$  and  $U_{\text{cal}}$  in Figure 6. Besides the expected second harmonic ( $n = 2$ ), Fourier decomposition of these two Stokes parameters for multiple consecutive sidereal days has also identified a weak sixth harmonic ( $n = 6$ ). Additionally, the Stokes  $I_{\text{cal}}$  and  $V_{\text{cal}}$ , which should have been constant and zero for a Gaussian beam, now contain a fourth harmonic ( $n = 4$ ). These artifacts are due to deviations of the realistic CST beam from a smooth Gaussian beam, which imply that Stokes parameters together can provide a direct means to further characterize the beam systematics.

### 3.3. Distortions from a Tilted Dipole

With such a large beam ( $\text{FWHM} \geq 60^\circ$ ) from the sleeved dipole, potential interactions between the ground soil and the antenna beam are expected, especially when the antenna had to be tilted at an angle of  $\delta_{\text{tilt}} = (90^\circ - \text{Observer Latitude})$  relative to the horizontal ground to point at the NCP.

As an example, the antenna model and its ground screen are tilted up by  $52^\circ$  relative to the ground soil slab in CST for an observing latitude of  $38^\circ\text{N}$ . The resulting beams (Figure 7), and their spectral gradients (Figure 8, right column) show that strong fringes across the band, which are the results of interferometric inter-

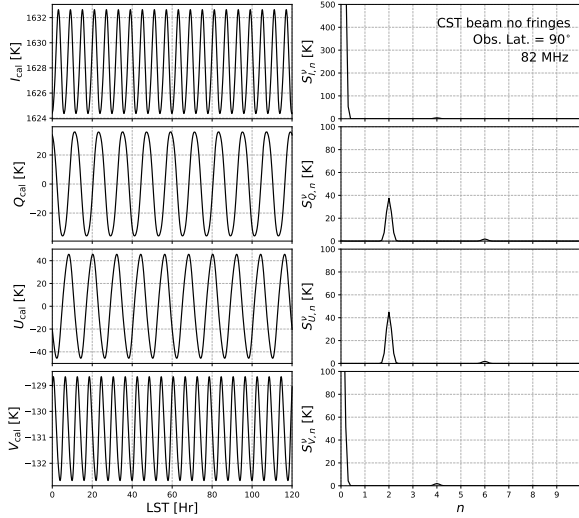


FIG. 6.— PIPE simulation result for the ground-parallel fiducial antenna beam at the GNP (Lat. =  $90^\circ\text{N}$ ). (Left) Temporal waveforms of the Stokes parameters (top to bottom:  $I_{\text{cal}}$ ,  $Q_{\text{cal}}$ ,  $U_{\text{cal}}$ ,  $V_{\text{cal}}$ ) for multiple sidereal days (as shown here for 7 days and 14 cycles). (Right) Harmonic decomposition for the corresponding Stokes parameters on the left, note the strong twice-diurnal ( $n = 2$ ) component for Stokes  $Q_{\text{cal}}$  and  $U_{\text{cal}}$ . Note that, although minute, imperfections on the CST beam give rise of the  $n = 4$  components for Stokes  $I$  and  $V$  as well as the  $n = 6$  components for Stokes  $Q$  and  $U$ .

actions between the antenna beam and the ground soil, have corrupted the beam smoothness.

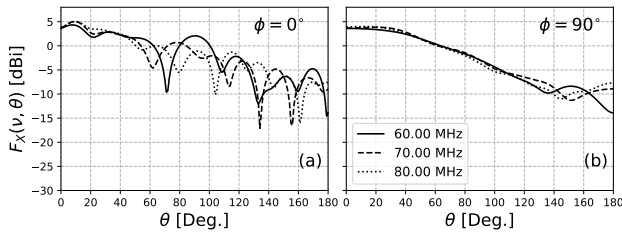


FIG. 7.— Angular plots for the CST beam of the sleeved dipole's  $X$ -polarization when the antenna is tilted toward the NCP. As a result, the  $E$ - and  $H$ -planes of the beam are corrupted by the fringing structures due to interferometric interactions with the ground soil when the antenna is tilted.

This can be understood through image theory, as illustrated in Figure 9. When a horizontal dipole antenna locates above a finite ground screen at height  $h$ , it produces a single image at the same distance under the ground plane. However, when titling the antenna and its ground screen toward the ground soil, the image below the soil and the one behind the antenna's ground screen no longer overlap. The interferometric interactions between these images subsequently imprint the unwanted fringes onto the beams. In fact, this effect is dependent on the antenna's directive gain since higher gain results in smaller FOV. This effect can be mitigated by placing the antenna on a slope with similar angle as the required tilting angle for NCP-pointing. Suspending or mounting the tilted antenna far from the ground can also help to reduce the fringing effects.

### 3.4. Horizon Obstruction at Lower Latitudes

In addition to the beam distortions, at a latitude of  $38^\circ\text{N}$ , the northern sky is partially obstructed by the

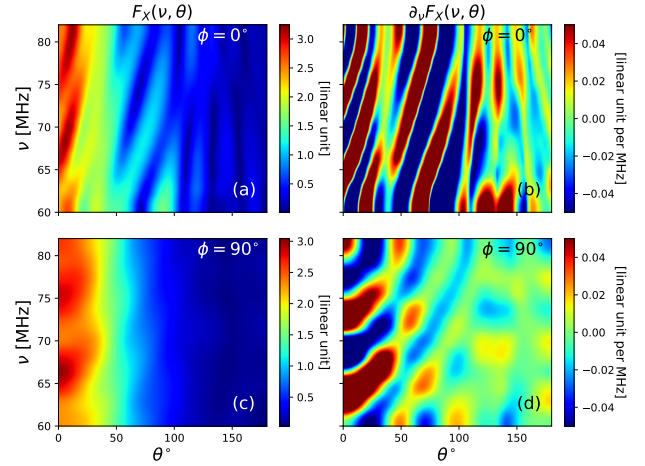


FIG. 8.— (Left) 2D plots of the  $E$ - and  $H$ -planes of the CST beam model,  $F_X(\theta, \phi, \nu)$ , when the sleeved dipole is tilted toward NCP. (Right) 2D plots of the frequency gradient,  $\partial_\nu F_X(\theta, \phi, \nu)$ , of the beams on the left panels. The strong fringing structures due to interactions between the beam and ground soil are more apparent in the gradient plots, with  $|\partial_\nu F(\theta, \phi, \nu)|$  exceeds 0.05.

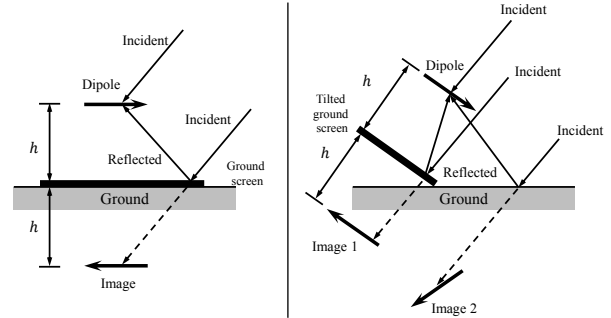


FIG. 9.— Illustration comparing image theory for the two antenna configurations. (Left) Zenith-pointing horizontal dipole above ground screen at height  $h$  produces a single image. (Right) Tilted dipole and ground screen relative to the ground soil can produce multiple images resulting in unwanted interferometric fringing which distorts the smooth beam pattern (Figure courtesy of NB17).

Earth's horizon. The continuously visible sky region over 24 sidereal hours is reduced when sky rises and sets over the horizon. As a result, in combination with distortions from the tilted beams, the smooth sinusoidal  $Q_{\text{cal}}$  and  $U_{\text{cal}}$  are replaced by waveforms with high-order harmonic components (Figure 10). There are still twice-diurnal components in Stokes  $Q$  and  $U$ , but their magnitude are reduced in the presence of the high-order terms. One possible mitigation strategy is to relocate the instrument to a higher latitude, closer to the geographic poles. This will help reducing the tilting angle thus ground interactions with the beam as described in the last section.

## 4. THE COSMIC TWILIGHT POLARIMETER

### 4.1. Instrumentation and Data Acquisition

The CTP adopted the sleeved dipole antenna design described in the previous section. The system electronics consisted of a thermally stabilized front-end (FE) stage along with a back-end (BE) instrument rack stored in a weatherproof and thermally regulated enclosure. The prototype was deployed during the Fall of 2017 at the Equinox Farm, LLC, in Troy, VA ( $38.0^\circ\text{N}$ ,  $78.3^\circ\text{W}$ ) as a testbed for the system integration, calibration, and pre-

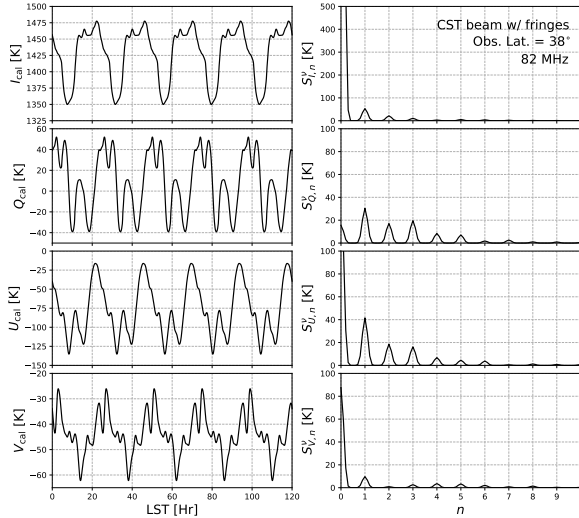


FIG. 10.— PIPE simulation result for CST antenna beam at 82 MHz located at  $38^\circ\text{N}$  which produces the horizon cutoff of the northern sky. (Left) Waveforms of the Stokes parameters (top to bottom:  $I, Q, U, V$ ) for multiple days of observation, note that the beam fringing effects and horizon cutoff have corrupted the symmetric sinusoidal waveforms from the idealized case. Instead they impose discontinuities and high-order harmonics to the waveforms. (Right) Fourier decomposition of the corresponding Stokes parameters from the left. The strong twice-diurnal components have been compromised by high-order terms.

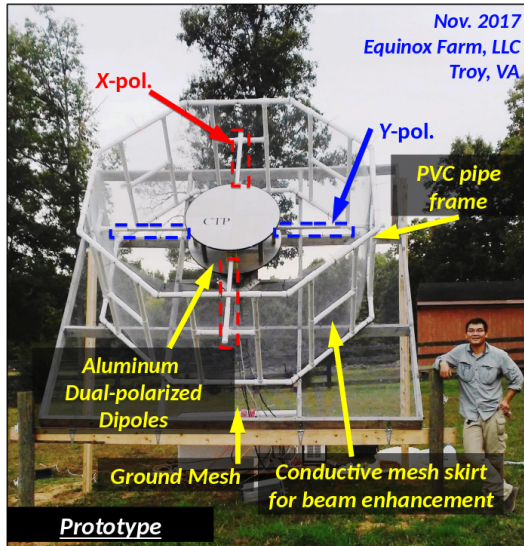


FIG. 11.— Front view of the tilted sleeved dipole antenna pointing at the NCP at the deployment site in Troy, VA at latitude of  $38.0^\circ\text{N}$ , on a  $\sim 10^\circ$  slope. The antenna was mounted on top of a temperature controlled enclosure for the FE electronics. The antenna was configured such that the Y-polarization (blue) is horizontally parallel to the ground, and X-polarization (red) is tilted toward the ground.

liminary measurement of the PIPE. The CTP used the Polaris during night time to align the pointing to the NCP. The general layout of the CTP is illustrated in Figure 11. Due to logistical constraints, we were only able to place the CTP on a shallow north-facing slope ( $\sim 10^\circ$ ) in an attempt to alleviate some of the ground interactions. The final tilting angle is about  $42^\circ$  from horizon.

The signal from each polarization was amplified by a low-noise amplifier (LNA) and filtered through a radio-

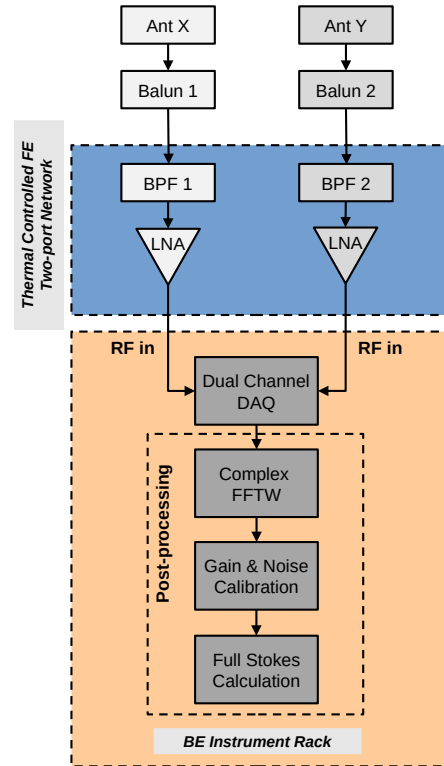


FIG. 12.— Block diagram for the CTP's instrument layout. The instrument FE (blue shaded) consists of a the thermal controlled stage for the main RF signal chain. The BE instrument rack consists of a FPGA-based signal digitizer. The sampled signal are channelized into spectrum with the FFTW program before the signal gain and noise temperature are corrected. In the end, Stokes parameters are calculated and monitored as a function of time before applying the harmonic decomposition on them for further analysis.

frequency (RF) module in the FE. Although the sleeved antenna was designed to operate between 60-120 MHz, a 30-MHz bandpass filter (BPF) centered at 75 MHz was used to reject radio frequency interference (RFI) from local digital TV stations and the FM band (88-108 MHz).

The output voltages from both polarizations were digitized by a FPGA-based analog-to-digital converter (ADC), Signatec PX14400A, before being channelized with fast Fourier transform (FFT), using the FFTW<sup>11</sup> software library, into complex voltages  $\tilde{V}_X(t, \nu)$  and  $\tilde{V}_Y(t, \nu)$  at a resolution bandwidth (RBW) of  $\Delta\nu \sim 57.00$  kHz. A block diagram for the instrument layout is provided in Figure 12.

Subsequently, the autocorrelation ( $\langle \tilde{V}_X \tilde{V}_X^* \rangle$ ,  $\langle \tilde{V}_Y \tilde{V}_Y^* \rangle$ ) and cross-correlation ( $\langle \tilde{V}_X \tilde{V}_Y^* \rangle$ ,  $\langle \tilde{V}_Y \tilde{V}_X^* \rangle$ ) were calculated and time averaged. The resulting uncalibrated net Stokes parameters were computed as

$$I_{\text{uncal}}(t, \nu) = \langle \tilde{V}_X \tilde{V}_X^* \rangle + \langle \tilde{V}_Y \tilde{V}_Y^* \rangle, \quad (9)$$

$$Q_{\text{uncal}}(t, \nu) = \langle \tilde{V}_X \tilde{V}_X^* \rangle - \langle \tilde{V}_Y \tilde{V}_Y^* \rangle, \quad (10)$$

$$U_{\text{uncal}}(t, \nu) = \langle \tilde{V}_X \tilde{V}_Y^* \rangle + \langle \tilde{V}_X^* \tilde{V}_Y \rangle, \quad (11)$$

$$V_{\text{uncal}}(t, \nu) = i \left( \langle \tilde{V}_X \tilde{V}_Y^* \rangle - \langle \tilde{V}_X^* \tilde{V}_Y \rangle \right). \quad (12)$$

<sup>11</sup> <http://www.fftw.org>, Frigo & Johnson (2005)

The Stokes parameters were converted to temperature units after calibrating for the multiplicative transducer gain,  $G_T(t, \nu)$ , and the additive instrumental noise temperature,  $T_n(t, \nu)$ , through the use of the network-theory based calibration equations with

$$I_{\text{cal}}(t, \nu) = \frac{1}{k_B \Delta \nu} \left[ \left( \frac{\langle \tilde{V}_X \tilde{V}_X^* \rangle}{G_{T,X}} + \frac{\langle \tilde{V}_Y \tilde{V}_Y^* \rangle}{G_{T,Y}} \right) - (T_{n,X} + T_{n,Y}) \right], \quad (13)$$

$$Q_{\text{cal}}(t, \nu) = \frac{1}{k_B \Delta \nu} \left[ \left( \frac{\langle \tilde{V}_X \tilde{V}_X^* \rangle}{G_{T,X}} - \frac{\langle \tilde{V}_Y \tilde{V}_Y^* \rangle}{G_{T,Y}} \right) - (T_{n,X} - T_{n,Y}) \right], \quad (14)$$

$$U_{\text{cal}}(t, \nu) = \frac{2}{k_B \Delta \nu} \frac{\text{Re}(\langle \tilde{V}_X \tilde{V}_Y^* \rangle)}{\sqrt{G_{T,X} G_{T,Y}}}, \quad (15)$$

$$V_{\text{cal}}(t, \nu) = \frac{-2}{k_B \Delta \nu} \frac{\text{Im}(\langle \tilde{V}_X \tilde{V}_Y^* \rangle)}{\sqrt{G_{T,X} G_{T,Y}}}, \quad (16)$$

where the subscripts in  $G_T(t, \nu)$  and  $T_n(t, \nu)$  refer to polarizations  $X$  and  $Y$ . The derivation of the calibration equations are provided in Appendix B and the procedures to determine  $G_T(t, \nu)$  and  $T_n(t, \nu)$  are described in the following section.

#### 4.2. Network-theory Based Calibration

In a conventional total-power experiment, one of the primary purposes of the calibration is to remove the multiplicative gain and additive noise temperature of the system to recover the apparent antenna temperature from the measured power. One of the simplest calibration schemes to implement is to correct the power gain and noise temperature for the sky signal power based on the measured power of a reference load. A Dicke radiometer calibration is one example based on such on-off reference load scheme (Dicke 1982). More sophisticated reference-load calibration schemes also rely on continuously recording and comparing the antenna power to the ones from multiple reference loads or a broadband noise source, such as the variants adopted by EDGES (Rogers & Bowman 2012) and SARAS (Patra et al. 2013).

In general, these calibration schemes assume the power gain and noise temperature of the system to be constant when toggling between the antenna and different reference calibrators over a short time interval. However, according to electrical network theory (Collin 2007; Engberg & Larsen 1995), a linear<sup>12</sup> two-port network (Figure 13), its power gain and noise temperature depend on the impedance of other devices connected at the network's input and output ports. Namely, the gain and noise temperature measured between the antenna and loads are not representative of one another since their impedance are not necessarily identical. Hence, deter-

<sup>12</sup> This is assumed if the device operates in the linear regime. For example, an active device like an LNA is not overdriven, which results in gain compression into the nonlinear regime.

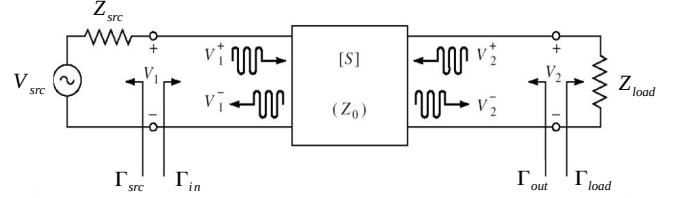


FIG. 13.— Diagram for a generic two-port network, with input source impedance  $Z_{\text{src}}(\nu)$  and output load impedance  $Z_{\text{load}}(\nu)$ . The incident ( $V^+$ ) and reflected ( $V^-$ ) voltages at the input and output ports are related by the scattering matrix  $\mathbf{S}(\nu)$  at some network characteristic impedance  $Z_0$ .  $\Gamma$  is the reflection coefficients due to the corresponding impedance at the given direction of the arrow.

mining the gain and noise temperature directly as a function of frequency can pose a challenge. For these reasons, a network-theory based calibration approach was adopted for the CTP. This scheme relies on impedance-independent network parameters to determine the power gain and noise temperature.

##### 4.2.1. Transducer Gain Correction with $S$ -Parameters

For a linear two-port network, the power gain can be described by the transducer gain  $G_T(\nu)$  as (Collin 2007),

$$G_T(\nu) = \frac{(1 - |\Gamma_{\text{src}}|^2)(1 - |\Gamma_{\text{load}}|^2)|S_{21}|^2}{|(1 - S_{11}\Gamma_{\text{src}})(1 - S_{22}\Gamma_{\text{load}}) - S_{12}S_{21}\Gamma_{\text{src}}\Gamma_{\text{load}}|^2}, \quad (17)$$

where  $S_{11}(\nu)$ ,  $S_{12}(\nu)$ ,  $S_{21}(\nu)$ , and  $S_{22}(\nu)$  are the complex components of the scattering matrix  $\mathbf{S}(\nu)$ . This set of  $S$ -parameters describes the intrinsic properties of the device under test (DUT) and can be measured directly with a Vector Network Analyzer (VNA) in the laboratory. Meanwhile,  $\Gamma_{\text{src}}(\nu)$  is the complex reflection coefficient of the DUT arising from impedance mismatch between the input source and the DUT's input port. Similarly,  $\Gamma_{\text{load}}(\nu)$  is the reflection coefficient caused by the mismatch between the network's output and a load<sup>13</sup> connected to the output port. The reflection coefficient is defined as  $\Gamma_i = (Z_i - Z_0)/(Z_i + Z_0)$ , where  $Z_0$  is the network's characteristic impedance.

For CTP, since the entire signal chain of each polarization (from the input of the FE modules through the output at the end of the coaxial cables before entering the digitizer) was considered as a single two-port network, end-to-end VNA measurements were made for the  $S$ -parameters. As a result, the  $S$ -parameters had also included the ohmic loss in the coaxial cables and other passive RF devices along the signal path before entering the digitizer.

It is worth pointing out that the  $G_T$  defined in Equation (17) has included the reflection efficiency terms due to impedance mismatch between the antenna and receiver as the first two terms in the numerator, i.e.,  $\eta_{\text{tot}}(\nu) = \eta_{\text{ant}}(\nu)\eta_{\text{rcv}}(\nu) = \eta_{\text{src}}(\nu)\eta_{\text{load}}(\nu) = (1 - |\Gamma_{\text{ant}}|^2)(1 - |\Gamma_{\text{rcv}}|^2)$  if the input source is the antenna and the output load is the receiver. On CTP, since the DUT's load is the digitizer whose input ports' impedance are well matched to the CTP's output ( $\sim 50 \Omega$ ), we assumed  $\eta_{\text{load}} \sim 1$ .

<sup>13</sup> The system load is distinct from the reference loads at the input port of the DUT. By definition, the load impedance refers to the one of any device connected at the output port of the device.



Furthermore, the  $S$ -parameters are functions of operating temperature since the electronic components are susceptible to thermal variations. To mitigate such fluctuations during observation, the CTP was equipped with an active thermal control system at the FE enclosure, using a thermoelectric Peltier cooler powered by a proportional-integral-derivative (PID) feedback circuit. Additionally, the  $S$ -parameters of the FE modules were measured with a VNA when operating at different set temperatures in a laboratory thermal enclosure, over a range of  $\sim 20$ - $35^\circ\text{C}$ .

These measurements helped to establish a thermal dependence for the  $S$ -parameters, which was used to correct for low-level temperature variations insensitive to the PID controller. Subsequently, a set of calibration coefficients were acquired by least-squares fitting these  $S$ -parameter measurements as functions of temperature and frequency. These coefficients helped to interpolate the  $S$ -parameters to an in situ ambient temperature  $T_{\text{amb}}$  recorded during each observation instance, which in return determined  $G_T(\nu, T_{\text{amb}})$  when  $\Gamma_{\text{src}}$  is substituted by  $\Gamma_{\text{ant}}$  measured in the field. Dependence of  $G_T(\nu, T_{\text{amb}})$  as a function of  $T_{\text{amb}}$  is shown in Figure 22 in Appendix C.

#### 4.2.2. Noise Temperature Correction with Noise Parameters

Analogous to  $G_T(\nu)$ , the noise temperature,  $T_n(\nu)$ , is also a function of the input source impedance  $Z_{\text{src}}(\nu)$ . It can be parametrized in terms of a set of four noise parameters intrinsic to the DUT, like the  $S$ -parameters. According to noise theory,  $T_n(\nu)$  reaches a minimum value at  $T_{\text{min}}(\nu)$  when the source impedance is matched to an optimal value  $Z_{\text{opt}}(\nu)$  as (Engberg & Larsen 1995),

$$T_n(\nu) = T_{\text{min}} + \frac{4NT_0|\Gamma_{\text{src}} - \Gamma_{\text{opt}}|^2}{|1 + \Gamma_{\text{opt}}|^2(1 - |\Gamma_{\text{src}}|^2)}, \quad (18)$$

where the dimensionless  $N(\nu) = R_n(\nu)G_{\text{opt}}(\nu)$  is the product of the equivalent noise resistance  $R_n(\nu) = \langle v_n^2 \rangle / (4k_B T_0 \Delta\nu)$  and the optimal source conductance  $G_{\text{opt}}(\nu)$ , with  $\langle v_n^2 \rangle$  is the mean-square noise-generator voltage and  $T_0 = 290 \text{ K}$ <sup>14</sup>. The complex source reflection coefficient and optimal impedance are defined as  $\Gamma_{\text{src}}(\nu)$  and  $\Gamma_{\text{opt}}(\nu)$  respectively. Including the real and imaginary parts of  $\Gamma_{\text{opt}}(\nu)$ , the set of noise parameters needed to determine  $T_n(\nu)$  for the CTP system is  $\{T_{\text{min}}(\nu), \text{Re}[\Gamma_{\text{opt}}(\nu)], \text{Im}[\Gamma_{\text{opt}}(\nu)], N(\nu)\}$ .

To determine the DUT's noise parameters, a set of  $T_n(\nu)$  were measured in the laboratory with a set of reference input fixtures consisting of simple passive electronic components ( $50 \Omega$ ,  $75 \Omega$ ,  $100 \Omega$ ,  $RC$ -circuit,  $RL$ -circuit). These fixtures provide source reflection coefficients more simple than the  $\Gamma_{\text{ant}}$  thus simpler frequency structures in  $T_n(\nu)$ . The four noise parameters were simultaneously fitted for the measured  $T_n(\nu)$  with the corresponding  $\Gamma_{\text{src}}(\nu)$  using the Python implementation of the Markov chain Monte Carlo (MCMC) sampler, `emcee`<sup>15</sup>. Combining with the field-measured  $\Gamma_{\text{ant}}(\nu)$ , these fitted noise parameters help to determine  $T_n(\nu)$  for the observational data. Details of this procedure and fitted noise parameters from different  $T_n(\nu, Z_{\text{src}})$  are illustrated in

<sup>14</sup> The standard noise temperature is conventionally defined to be 290 K so that  $k_B T_0 \approx 4.00 \times 10^{-21} \text{ W}$ s.

<sup>15</sup> <http://dfm.io/emcee/current/>

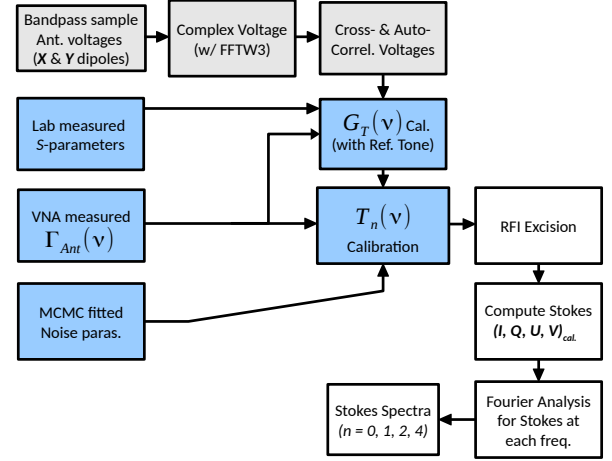


FIG. 14.— Block diagram for the data pipeline for acquisition (gray shaded boxes), calibration (blue shaded) and reduction (white).

Appendix C.

#### 4.3. Preliminary Polarization Constraints

Since the CTP was deployed outside the radio-quiet zone, the observed spectra were expected to be contaminated by RFI. Although the BPF between 60-90 MHz has substantially reduced the RFI from the FM band, majority of the band was still corrupted. Nonetheless, a small subband around 82 MHz was determined to be the cleanest for the preliminary analysis.

As summarized in Figure 14, after applying the aforementioned calibration for  $G_T(\nu)$  and  $T_n(\nu)$ , kurtosis-based RFI excision was applied to the auto- and cross-correlated voltages for the two polarizations before computing the Stokes parameters<sup>16</sup> FFTs were then applied to the four Stokes parameters to extract the harmonic components. In order to resolve any underlying harmonics, the time data length needs to be increased. In practice, multiple consecutive days of data will be concatenated into single data streams prepared for the FFT.

Within the 10 days of observation, the 24 hours of data collected on Dec 1<sup>st</sup>, 2017 are the least contaminated by RFI and other spurious distortions. To achieve the needed resolution for the low-order harmonics in the Stokes PSD, that single day of data were duplicated for 10 times to emulate 10 days of continuous observation. Additionally, to suppress some of the high-frequency noise in the observed data, a Savitzky-Golay filter was applied to concatenated data streams as a moving mean before computing the FFT.

The window size of the filter was chosen to be around 2% of the total data length. Since the larger the window size is, the more high-order harmonics are filtered out. After comparing different window sizes, the 2% window width was determined to provide a good balance

<sup>16</sup> To constrain the PIPE in the tilting configuration, no beam correction were applied when comparing the observed Stokes with simulation. However, to properly correct the beam pattern, CST simulation will be needed. The CST beams have included the ohmic loss when proper materials are assigned to the detailed antenna model. The antenna ohmic loss can be constrained through the ohmic loss efficiency  $\epsilon_r(\nu)$  provided in CST, where typically the lossy antenna effective area is defined as  $A_e(\text{lossy}) \sim \epsilon_r A_e(\text{lossless})$ .

TABLE 1  
OBSERVED AND SIMULATED STOKES HARMONICS AT 81.98 MHz

	$S_{i,1}$ [K]	$S_{i,2}$ [K]	$S_{i,3}$ [K]	$S_{i,4}$ [K]
Obs.				
$I$	$71.53 \pm 8.66$	$53.05 \pm 8.66$	$46.98 \pm 8.66$	$11.33 \pm 8.66$
$Q$	$74.08 \pm 5.75$	$18.85 \pm 5.75$	$8.95 \pm 5.75$	$6.10 \pm 5.75$
$U$	$43.59 \pm 3.44$	$25.46 \pm 3.44$	$24.81 \pm 3.44$	$5.22 \pm 3.44$
$V$	$48.42 \pm 4.96$	$39.47 \pm 4.96$	$49.57 \pm 4.96$	$5.57 \pm 4.96$
Sim.				
$I$	61.38	30.23	19.44	11.72
$Q$	35.84	22.73	25.08	14.09
$U$	45.01	21.86	19.51	10.12
$V$	14.75	5.84	7.59	8.50
Ratio	Obs./Sim.			
$I$	$1.17 \pm 0.22$	$1.75 \pm 0.58$	$2.42 \pm 1.17$	$0.97 \pm 1.03$
$Q$	$2.07 \pm 0.37$	$0.83 \pm 0.33$	$0.36 \pm 0.24$	$0.43 \pm 0.44$
$U$	$0.97 \pm 0.11$	$1.16 \pm 0.24$	$1.27 \pm 0.29$	$0.52 \pm 0.38$
$V$	$3.28 \pm 1.15$	$6.76 \pm 5.80$	$6.53 \pm 4.32$	$0.66 \pm 0.70$

between preserving the fidelity of the lowest four harmonics ( $n \geq 4$ ) and rejecting some of the noise as well as discontinuities due to RFI excision. The window-size optimization process is illustrated in Figure 24 in Section C.2.

The PIPE simulation suggests that no significant harmonics should appear for  $n \geq 10$ . The confidence intervals of the harmonics are standard deviations of the Stokes PSD for  $n \geq 10$  before applying the Savitzky-Golay filter. They are computed as,

$$\hat{\sigma}_{S_i}^2 = \frac{1}{(n_{\max} - n_{\min} + 1)} \sum_{n=n_{\min}}^{n_{\max}} (S_{S_i,n}^\nu - \hat{\mu}_{S_i}^\nu)^2, \quad (19)$$

where the estimated sample mean of the noise floor in the Stokes PSD is determined by,

$$\hat{\mu}_{S_i}^\nu = \frac{1}{(n_{\max} - n_{\min})} \sum_{n=n_{\min}}^{n_{\max}} S_{S_i,n}^\nu, \quad (20)$$

with  $[n_{\min}, n_{\max}] = [10, N]$ .

Magnitudes of the identified harmonics at  $n = \{1, 2, 3, 4\}$  and corresponding uncertainties  $\hat{\sigma}_{S_i}$  in the Stokes waveforms are listed in Table 1 and shown in Figure 15. From the observed data, the signal-to-noise ratio (S/N) at the twice-diurnal components in Stokes  $Q$  and  $U$  are computed to be 3.27 and 7.40, respectively.

Relative magnitude ratios between the observed low-order harmonics and ones from PIPE simulation at 81.98 MHz are also presented in Table 1. The observed harmonics for  $n = \{1, 2, 3\}$  in Stokes  $U$  are the most consistent to the simulation (with their ratios close to unity within uncertainty). Meanwhile  $S_{I,1}$  is also consistent with the simulation since this represents the bulk part of the diurnal component when the Galaxy rises and sets. However, Stokes  $Q$  and  $V$  are stronger in the observation.

These discrepancies most likely arose from the observed stronger signal measured in polarization  $Y$  (horizontally oriented) comparing to  $X$  (Figure 11). Additional signal could also have been reflected and scattered off the ground when the antenna was tilted forward. Since Stokes  $Q$  was computed as the difference between the autocorrelated power of  $X$  and  $Y$  in Equation (10), uneven signal power measured between dipole  $X$  and  $Y$  could introduce an offset to Stokes  $Q$ . Some of the scattered signal might have also contributed to the circular

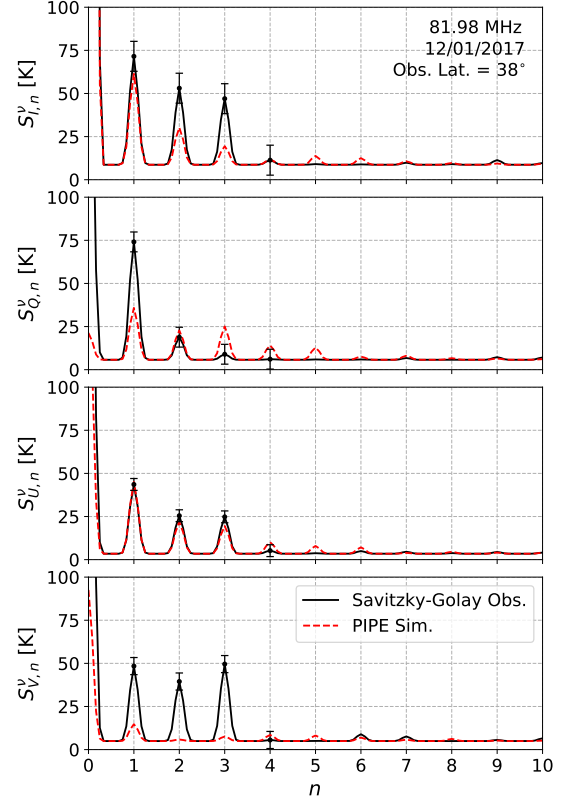


FIG. 15.— Comparison of the harmonic decomposition, up to  $n = 10$ , between the observation (black curve) and PIPE simulation with the tilted beam and horizon cutoff (red curve) at  $\sim 82$  MHz. To better compare PSD of the Stokes waveforms smoothed by the Savitzky-Golay filter, the observation noise  $\hat{\sigma}_{S_i}$  was added to the noiseless PIPE simulation in the analysis.  $S_{Q,n}^\nu$  and  $S_{U,n}^\nu$  strongly indicate there is induced polarization observed in the data. However, due to the limited number of clean channels, further evaluation is needed when the CTP is redeployed to a more RFI-quiet environment. Note that there is a slight shift in the observed harmonics comparing to the simulation, this is determined to be inaccuracy in cadence when concatenating multiple days of data into a single data stream for the FFT computation.

polarization as seen in the stronger Stokes  $V$  harmonics (Figure 11). Follow-up studies are needed to further evaluate these effects.

## 5. OTHER SYSTEMATICS

### 5.1. Beam Chromaticity and Spectral Smoothness

By definition, the sky-averaged antenna temperature  $T_{\text{ant}}(\nu)$  in Equation (7) is a beam-weighted value of the sky brightness temperature  $T_{\text{sky}}(\theta, \phi, \nu)$ . Consequently, despite the intrinsic spectral smoothness of the sky-averaged foreground spectrum, the observed sky spectrum is corrupted by the spectral variations in the beam patterns. This can potentially introduce unknown absorption or emission features to the residual spectrum after removing the foreground component using a foreground fitting model like Equation (1).

Although antenna simulations from CEM software, like CST, HFSS<sup>17</sup>, FEKO<sup>18</sup>, can provide detailed antenna beam patterns to aid the beam chromaticity assessment and calibration (e.g., Bernardi et al. 2015; Mozdzen et al.

<sup>17</sup> <https://www.ansys.com/Products/Electronics/ANSYS-HFSS>

<sup>18</sup> <https://www.feko.info/>

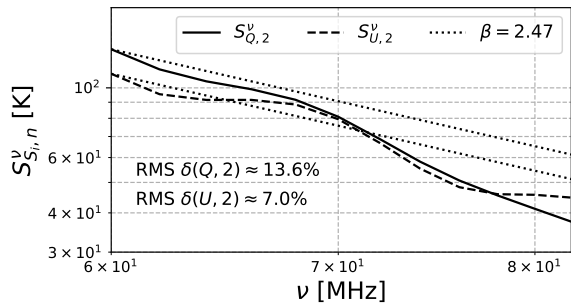


FIG. 16.— Stokes spectra from the ground-parallel fiducial beam model indicate that the beam chromaticity of the antenna beam has distorted the smooth power-law input foreground model with spectral index of  $\beta = 2.47$ . The beam spectral structures on the Stokes spectra, with RMS errors between 13% ( $S_{Q,2}^\nu$ ) and 7% ( $S_{U,2}^\nu$ ), complicate the direct use of the Stokes spectra to constrain the foreground spectrum, unless the beam structures are understood and corrected.

2016). Others have adopted a mitigation approach by optimizing the antenna design to achieve smoother frequency response (both in the beam pattern and antenna reflection coefficient  $\Gamma_{\text{ant}}$ ) over a large frequency range, such as the blade antenna from EDGES II (50-100 MHz, Mozden et al. 2016) or the spherical monopole from SARAS 2 (110-200 MHz, Singh et al. 2017). Nonetheless, decoupling the beam dependence from the beam-weighted measurement of  $T_{\text{ant}}(\nu)$  is an inverse problem. This process is nonlinear mainly due to the lack of detailed spatial information of the sky and the beam patterns in a single total-power measurement.

Similarly, the PIPE Stokes measurements are also susceptible to spectral variations in the antenna beams, as evident in Equations (3)-(6). In Figure 16, PIPE simulations with the fiducial beam indicates that the second-harmonic Stokes spectra,  $S_{Q,2}^\nu$  and  $S_{U,2}^\nu$ , can no longer simply track the foreground power-law model with spectral index  $\beta = 2.47$  as with the idealized Gaussian beams.

The spectral distortions imprinted by the fiducial beam patterns on the simulated Stokes spectra are quantified by computing an overall RMS value across the band for the relative error between the simulated foreground spectrum with the power law as,

$$\delta(S_i, n, \nu) = 100\% \times \left| \frac{S_{S_i, n}^\nu - \hat{S}_{S_i, n}^\nu}{\hat{S}_{S_i, n}^\nu} \right|, \quad (21)$$

where  $\hat{S}_{S_i, n}^\nu$  is the power law spectrum, computed with  $\beta = 2.47$ ,

$$\hat{S}_{S_i, n}^\nu = S_{S_i, n}^{\nu_0} \left( \frac{\nu}{\nu_0} \right)^{-\beta}, \quad (22)$$

normalized at frequency  $\nu_0$ , which was chosen to be the lower end of the band, at 60 MHz. This metric simply describes the deviation from the expected sky power law in the presence of beam chromaticity.

The RMS errors of the second-harmonic Stokes spectra relative to the smooth power law are 13.6% and 7.0% for Stokes  $Q$  and  $U$  respectively, with the spectral gradient for this beam satisfying  $|\partial_\nu F(\theta, \phi, \nu)| \geq 0.05$ . These distortions, which are contributed by the Mueller components  $M_{21}(\Omega, \nu)$  and  $M_{31}(\Omega, \nu)$ , imply that an antenna

with smoother response is needed to replace the existing sleeved dipole. Nevertheless, some degree of beam calibration is still needed. Since correcting for the  $M_{21}$  and  $M_{31}$  is also a nonlinear process, it is difficult to account for the beam effects in the twice-diurnal spectra analytically. A SVD-based analysis approach, as summarized in Section 6, has shown promising potential in constraining the foreground spectrum more reliably when simultaneously taking into account all four Stokes parameters along with a priori training sets for foreground maps and beam models.

## 5.2. Foreground Spectral Index Variations

It is well known that the spectral index for the estimated foreground power-law spectrum varies with position and increases with frequency, i.e.,  $\beta = \beta(\Omega, \nu)$  (Kogut 2012). For example, by extrapolating a power law between the Haslam sky map at 408 MHz to the Guzmán map at 45 MHz (Guzmán et al. 2011), it is clear that the derived spectral indices vary between 2.3 on the galactic plane and 2.8 at high galactic latitudes (Figure 17). By comparing different surveys between 22 MHz and 1.4 GHz, Kogut (2012) finds that the mean spectral index increases by  $\Delta\beta \sim 0.07$  per octave in frequency. Hence, the spectrum's spectral index was assumed constant over a small subband (such as 30-MHz band on the CTP) in the PIPE simulation. However,  $\beta$ 's spatial variations are still need to be accounted for.

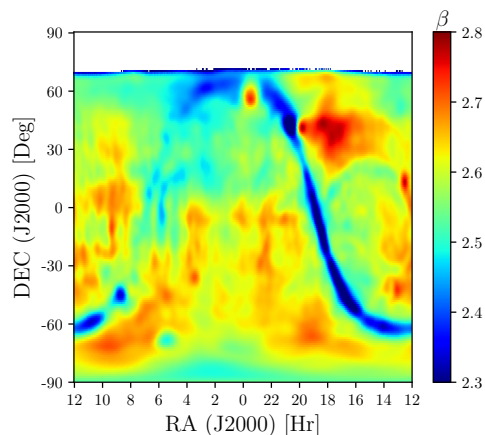


FIG. 17.— Foreground spectral index distribution is obtained from extrapolating between the Haslam all-sky survey at 408 MHz and a 45 MHz map from Guzmán et al. (2011). The missing data around the NCP represents  $\sim 4\%$  of the whole sky in the 45-MHz map.

It is apparent, from Equations (3)-(6), that the level of sky modulation on the PIPE depends on the sky pointing. When the CTP's zenith-pointing coincides with the NCP, as in the fiducial model from Section 3.2, only a single value of the mean spectral index is measured in Stokes  $I_{\text{net}}(t_{\text{LST}}, \nu)$  due to the constant FOV in this configuration. Meanwhile the remaining three Stokes parameters are modulated by the two-fold symmetry pattern in  $M_{21}(\Omega, \nu)$  and  $M_{31}(\Omega, \nu)$  and four-fold ones in  $M_{41}(\Omega, \nu)$  (Figure 2), the spatially dependent spectral

index can affect them as

$$S_{i,\text{net}}(\nu) \propto \int_{\Omega} d\Omega M_{(i+1)1}(\Omega, \nu) I_{\text{sky}}(\Omega, \nu_{\text{map}}) \left( \frac{\nu}{\nu_{\text{map}}} \right)^{-\beta(\Omega)} \quad (23)$$

where  $S_{i,\text{net}}$  with  $i = \{1, 2, 3\}$  represent  $\{Q_{\text{net}}, U_{\text{net}}, V_{\text{net}}\}$ , and  $\nu_{\text{map}}$  is the reference frequency at which the sky map  $I_{\text{sky}}$  is measured.

Although extrapolation between sky maps at different frequencies can help to constrain  $\beta(\Omega, \nu)$ , corrections for observational systematics and spatial resolutions among different sky surveys can be challenging, not to mention that not all surveys are able to cover the entire sky like the Haslam map (de Oliveira-Costa et al. 2008). It will be invaluable to complement them with physically motivated all-sky models, such as the Global Sky Model (GSM, de Oliveira-Costa et al. 2008), and the Global Model for the Radio Sky Spectrum (GMOSS, Sathyanarayana Rao et al. 2017b), into the analysis for the PIPE.

### 5.3. Foreground Intrinsic Polarization

In Section 2, the PIPE is formulated by assuming unpolarized incoming signal. The diffuse Galactic synchrotron emission is known to be linearly polarized. However, this intrinsic foreground polarization has been determined to be relatively weak at arcmin-scaled angular resolution, hence is not expected to be a major contaminant (Bernardi et al. 2009, 2010). Additionally, due to the ionospheric fluctuations, the contribution from intrinsic foreground polarization is expected to be randomized and averaged in a sky-averaged measurement. Nonetheless, the effect of intrinsic polarization can be characterized in future PIPE simulations simply by including the small regional sky polarization surveys (e.g., Wolleben et al. 2006; Testori et al. 2008) or physically-motivated all-sky polarization simulations (e.g., Waelkens et al. 2009; Jelić et al. 2010) along with the complete  $4 \times 4$  Mueller matrix in Equation (A7).

### 5.4. Ionospheric Effects

Ionospheric activities are generally related to the diurnal solar cycle. Their bulk effects, due to electron density fluctuations, are enhanced during daytime, meanwhile small-scale structures are typically strongest during twilight and nighttime. The ionosphere can be considered in terms of equatorial, mid-latitudes, and polar regions (Sukumar 1987). Ionospheric effects due to large-scale fluctuations in electron density are strongest in the equatorial and mid-latitudes, whereas effects from small-scale structures tend to appear more in the equatorial and polar regions.

There are four common ionospheric effects that need to be considered: refraction, absorption, attenuation, and scintillation. Total electron content (TEC) fluctuations in the large scale structure of the ionosphere ( $\sim 10$ -100s km) can alter transmission properties of the medium and propagation direction of the incoming radio signal. Some of the previous studies have suggested that ionospheric refraction and absorption due to TEC fluctuations can have long-term effects on the sensitivity of the observations, such as increase in  $1/f$  noise (Vedantham et al. 2014; Datta et al. 2016). Meanwhile, another study has

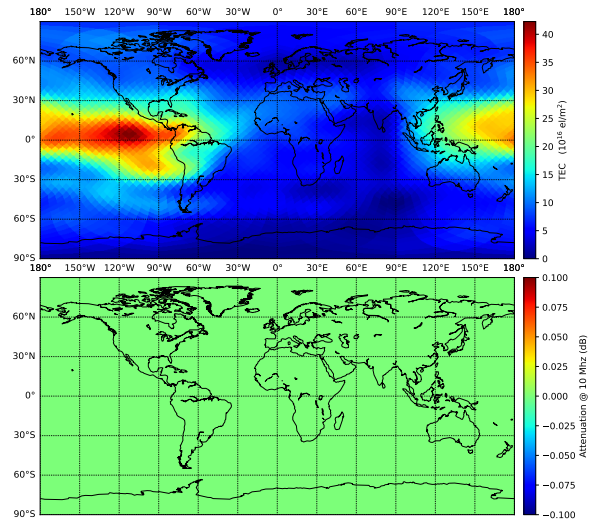


FIG. 18.— TEC (top) and attenuation (bottom) maps for the ionosphere conditions on normal day (Sept 01, 2017 at 00:00 UTC). Although there are large variations TEC close to the Equator, which is typical, no significant attenuation is observed. Source: CODE and NOAA.

pointed out that such variability does not pose a significant problem for ground-based global 21 cm experiments as long as the data are randomized and averaged at a time interval shorter than the characteristic time scale of the ionospheric  $1/f$  noise (Sokolowski et al. 2015b). Nonetheless, since the harmonic analysis of the PIPE Stokes relies on concatenating multiple consecutive days of data, long-term effects of the ionospheric fluctuations will need to be characterized and corrected. One possible remedy is to align and randomize the data of each day in LST. The sky-modulated PIPE waveforms should be preserved.

On the other hand, if one desires to mitigate the horizon obstruction by observing at latitudes closer to the geographic poles, attenuation from the ionosphere will be more dominant, especially during strong solar activity such as flares and coronal mass ejections (CME). By comparing the archival TEC data<sup>19</sup> along with the attenuation maps<sup>20</sup> between a normal day (Sept 01, 2017 at 00:00 UTC, Figure 18) and a day with a strong flare (Sept 09, 2017 at 23:00 UTC, Figure 19), it is apparent that majority of the ionosphere in polar regions is saturated during the flare day, which leads to complete attenuation of the sky signal. However, the occurrence of these events is infrequent, hence can be flagged and removed from the data if needed. Note that the attenuation and TEC level do not necessarily correlate.

Furthermore, there is also ionospheric scintillation, which appears as small scale variations ( $\sim 1$  m to tens of km), can cause rapid disruptions on the RF signal's amplitude and phase coherency (van Bommel 2007) and result in noise-like terms in the observed spectrum. These

<sup>19</sup> Data provided by the Center for Orbit Determination in Europe (CODE), fetched by the Python script `radionopy` provided by Prof. James Aguirre from the University of Pennsylvania, <https://github.com/UPennEoR/radionopy>

<sup>20</sup> Attenuation maps are based on Sauer & Wilkinson (2008) data, acquired from the National Oceanic and Atmospheric Administration (NOAA): <https://www.swpc.noaa.gov/content/global-d-region-absorption-prediction-documentation>

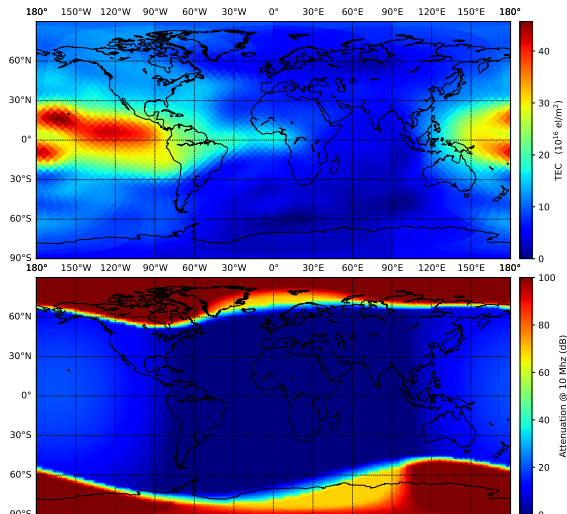


FIG. 19.— TEC (top) and attenuation (bottom) maps for the ionosphere conditions on the day with a strong solar flare (Sept 09, 2017 at 23:00 UTC). During the active period, ionosphere in both polar regions (latitude  $\geq 60^\circ$ ) are saturated with high energy particles so that the signal are large attenuated. Although this is not ideal for any experiments located at those latitudes, these solar activities are neither frequent nor long-lasting. Hence, it is not a major threat for any ground-based experiments close to the poles. Source: CODE and NOAA.

variations may also help to scramble the intrinsic foreground polarization through changes in the amount of Faraday rotation as mentioned in the last section.

## 6. IMPLICATIONS ON 21 CM BACKGROUND SIGNAL EXTRACTION

By now, it is evident that the PIPE is more complex than the simplistic Gaussian beam simulation in NB17, especially in the presence of instrumental systematics on the beams and intrinsic spectral properties of the foreground synchrotron emission. Other global experiments have utilized elaborate receiver calibration schemes, detailed CEM beam models, and antenna designs with smoother responses, to mitigate spectral distortions on the observed spectrum. Nonetheless, uniqueness can be a concern when trying to correct for all these systematics from a single averaged total-power spectrum.

One advantage of the sky-modulated PIPE over a single total-power spectrum is the additional constraints on the foreground and antenna beam characteristics imprinted in the full-Stokes measurement. In principle, if all four Stokes measurements are constrained simultaneously, the robustness and accuracy of separating of the foreground spectrum from the weak 21 cm signal will improve. Furthermore, underlying instrumental and observational systematics can be accounted for if the observed signal can be decomposed into different components (or modes) and compared to a priori information of the expected systematics. An SVD-based analysis provides such a means.

In brief, the SVD algorithm decomposes the observed sky-modulated PIPE signal and simulation into two different sets of eigenmodes. Ones corresponding to the foreground and systematics in the observation can be isolated and removed based on the modes appear in the simulated data. Statistical uncertainties of the systematic components introduced to the simulated data are constrained by a priori training data sets. Subsequently,

remaining eigenmodes in the observed signal allow the background signal of interest to be reconstructed and statistically bounded by theoretical global 21 cm models.

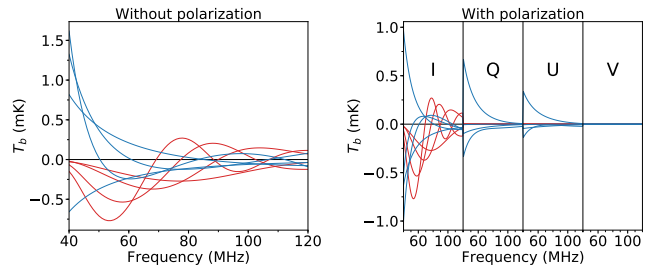


FIG. 20.— Illustration of the SVD basis functions for the simulated total power alone (top), and with induced polarization (bottom). When decomposing the total power alone, the overlapping between the modes for injected 21 cm background signal (red) and the foreground spectrum (blue). However, since the foreground is solely responsible for the induced polarization, the SVD modes in Stokes  $Q$  and  $U$  provide the needed additional constraints on the foreground.

As an example, the SVD algorithm, as implemented in the Python code `pylinex`<sup>21</sup> (Tauscher et al. 2018b), was applied to the fiducial PIPE simulation described in Section 3.2, embedded with an additional global 21 cm model generated by the ARES<sup>22</sup> (Mirocha 2014) code. Statistical training sets for the beam-weighted foreground were constructed by convoluting the scaled Haslam map with a series of CST beams consisting of different model perturbations (e.g., thermal expansions on different components on antenna structure, ground soil properties and thickness, ground screen characteristics). Meanwhile, a collection of global 21 cm models was generated using the ARES code with different combinations of neutral hydrogen fraction  $x_{\text{HI}}(z)$  and 21 cm spin temperatures  $T_{s,21\text{cm}}(z)$ . Also, as a blind test, the specific global 21 cm model embedded in the PIPE test signal was left out of the training set.

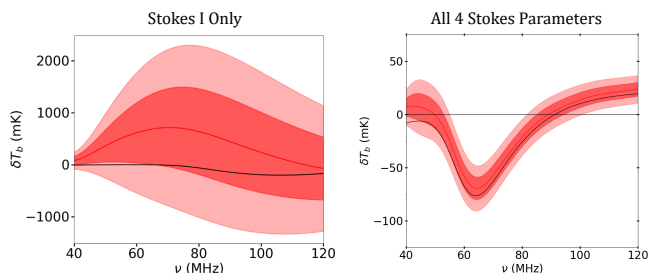


FIG. 21.— By utilizing a large training set of global 21 cm signal, simulated beam models, and the Haslam map, the SVD-based `pylinex` code demonstrates the power of the PIPE approach when simultaneously constraining all four Stokes parameters (right) instead of just the total-power spectrum as in the conventional approach (left). The two uncertainty bands are  $1\sigma$  (dark red) and  $2\sigma$  (light red) of the recovered signal (solid red curve), overplotted on top of the input global 21 cm model (solid black curve). Note also the scales between the two panels are at least an order of magnitude different.

The SVD eigenmodes of a simulated single total-power

<sup>21</sup> <https://bitbucket.org/ktausch/pylinex>

<sup>22</sup> The Accelerated Reionization Era Simulation, <https://bitbucket.org/mirocha/ares>

spectrum are contrasted with the full-Stokes counterpart in Figure 20. When the additional Stokes data are included, distinctions between the foreground and background signal’s eigenmodes are more prominent as the eigenmodes corresponding to the foreground components only present in Stokes  $Q$  and  $U$ . Hence, the foreground and beam effects can be identified more easily. As a result, the reconstructed 21 cm signal from the all-Stokes spectra is more robust and precise than the single total-power spectrum, as illustrated in Figure 21.

The robustness of this analysis for separating unwanted data components from the 21 cm background can be quantified by checking the goodness of the fit to the data through either the traditional reduced chi-squared statistic or the newly devised psi-squared statistic (Tauscher et al. 2018a). If a goodness of fit threshold is not met, modifications to the PIPE simulation, such as including extra systematics and training sets, may be required before the SVD analysis process restarts. Additionally, determining an optimal number of modes for each of the signal components plays a key role in the success of the SVD approach. Tauscher et al. (2018b) show that minimizing the Deviance Information Criterion (DIC) best optimizes the number of modes to use for each training set or data component. Follow-up studies are under way to apply similar SVD analysis on new observation data.

## 7. CONCLUSION AND FUTURE WORK

In this study, we review different implementation aspects of the newly proposed polarimetry-based observational technique, using sky modulation for the Projection-Induced Polarization Effect (PIPE), to constrain the foreground spectrum for global 21 cm cosmology. Simulation of the PIPE has been extended to include realistic beam effects, such as beam chromaticity, beam distortions from ground soil, and Earth’s horizon obstruction. In conjunction, the Cosmic Twilight Polarimeter (CTP) is presented as a testbed instrument for implementing the network-theory based calibration scheme and the sky-modulated PIPE observation by tilting a broadband sleeved dipole’s pointing toward the NCP at a latitude of  $38^\circ\text{N}$ .

Instead of reference-load switching, the CTP has adopted a network-theory based calibration scheme to correct for the power transducer gain,  $G_T(\nu)$  and noise temperature,  $T_n(\nu)$ . Instead of attempting to determine these two variables directly, since both are functions of the antenna reflection coefficient  $\Gamma_{\text{ant}}(\nu)$ , two sets of intrinsic system variables ( $S$ -parameters and noise parameters) are measured. Subsequently,  $G_T(\nu)$  and  $T_n(\nu)$  of the observing system are computed by substituting  $\Gamma_{\text{ant}}(\nu)$  into the parametrization formulae of the network parameters.

Despite strong RFI contamination across the 60-90 MHz band and most of the observational data, by duplicating and concatenating one of the cleanest days of data to emulate a continuous observational data set, a desired FFT resolution for the low-order harmonics was achieved. Preliminary analysis of the harmonics, compared to the PIPE simulation, suggests the presence of a twice-diurnal component in the net Stokes parameters around 82 MHz, specifically in the Stokes  $U$ . Based on the estimated statistics in the observation, S/N of the twice-diurnal components in Stokes  $Q$  and  $U$  are 3.27

and 7.40 respectively. Importantly, the observed harmonics in Stokes  $U$  are consistent with the PIPE simulation since their ratios for  $n = \{1, 2, 3\}$  are unity within uncertainty. However, there are discrepancies between the observation and simulation, such as ones in other Stokes parameters  $Q$  and  $V$ , mainly due to RFI corruptions, small sample size, and unknown systematics.

Among the discussed systematics, the following contribute the most to spectral distortions in the sky-modulated PIPE measurements:

1. Similarly to the total-power measurement, the beam chromaticity also affects the PIPE Stokes antenna temperatures. Although dynamical sky modulation provides a unique way to constrain the foreground component, beam chromaticity imprinted in the Stokes parameters needs to be corrected. Hence, constraining the foreground spectrum using the Stokes parameters becomes more complicated than the idealized procedure proposed in NB17.
2. Simply tilting the antenna forward, as in the CTP prototype presented here, is not recommended when the antenna is close to the ground. Nearfield interactions with the ground soil can corrupt the beam pattern’s smoothness (Section 3.3). Having the antenna situated on a slope or suspended off the ground when tilted will alleviate these corruptions. Additionally, FOV obstruction from the Earth’s horizon can be reduced by relocating the instrument closer to the geographic poles, thus decreasing the antenna’s tilting angle and suppressing the ground interactions.
3. Spatial distribution of the foreground spectral index  $\beta(\Omega)$  also affects the accuracy of the recovered foreground spectrum using the sky-modulated PIPE. When no longer sharing a uniform spectral index across the sky, each Stokes parameter is only sensitive to the given sky region modulated by the corresponding Mueller pattern, as described in Equation (23). Hence, the net Stokes  $Q$  and  $U$  can produce foreground spectra with slightly different frequency dependence than the foreground in Stokes  $I$ .

Nonetheless, the SVD-based `pylinex` code provides a promising background signal extraction procedure when using statistical training sets to address some of the intrinsic foreground and instrumental systematics, such as the three above. Preliminary analysis on the simulated data indicates that it is plausible to extract the background 21 cm signal as long as training sets with a priori information on the foreground, antenna beam, electronics calibration, and other systematics are sufficiently well defined (through sky survey maps and models like GMOSS, CST beam models, and laboratory measurements of  $S$ - and noise-parameters, respectively).

Instead of requiring precise knowledge of the foreground and instrumental effects, `pylinex` constrains the background 21 cm signal by decomposing the training sets of each possible data component into eigenmodes. By simultaneously fitting them to the full-Stokes measurements, the algorithm provides a well-informed separation between background, foreground, and systematics.

The goodness of fit to the observation can be optimized with the reduced chi-squared or psi-squared statistics. The order of SVD eigenmodes to be used for each training set is optimally determined by minimizing an information criterion such as the DIC.

Although preliminary CTP observation has shown evidence of sky-modulated PIPE, a follow-up effort is necessary to improve the sensitivity of the data, such as relocating the system to the Green Bank Observatory (GBO, 38.4°N, 79.8°W) inside the radio quiet zone in West Virginia. Although the presented calibration is sufficient for the induced polarization, the CTP system is currently being upgraded and refined to improve the sensitivity of the gain and noise calibration for the global 21 cm science (which is at least three orders of magnitude lower than the induced polarization). Detailed component-level network models are being constructed for the front-end and receiver using the Keysight's Advanced Design Simulation (ADS) electronic design software. The network models will help to validate the calculated transducer gain and noise temperature when the input ports are subjected to the antenna impedance. Additionally, a new broadband and dual-polarized antenna design with a smoother frequency response is being explored to reduce spectral distortions from the beam pattern, along with reviewing possible modifications on the existing sleeved dipole for comparison.

Another possible path, to mitigate the ground distortions on the tilted beam, is to point the antenna at the zenith instead of at the celestial pole when observing at the GBO. This approach will significantly decrease the sensitivity in detecting the twice diurnal waveforms in the Stokes parameters compared to when observing at the poles. However, the pattern recognition technique implemented in `pylinex`, in combination with suitable training sets, may be able to take advantage of the complete information provided by full-Stokes measurements. Although this may resemble conventional global 21 cm experiments, to the best of our knowledge, no other

single-element total-power global experiment has incorporated polarimetry and pattern recognition together. With the upgraded CTP, applications of a pattern recognition method on both the drift-scanning total-power and the dynamic PIPE measurements can be fully evaluated, for the first time with observational data.

Moreover, there is also great potential for adopting the induced polarization approach on a future space-based mission since many of the ground-based challenges, such as ground interactions with the antenna beam and horizon obstruction, as well as ionospheric effects, will be eliminated. In fact, previous studies (e.g., Burns et al. 2012, 2017; Falcke et al. 2018) have suggested that the lunar farside is the optimal location for such an experiment due to its pristine radio-quiet environment within the inner solar system.

## 8. ACKNOWLEDGMENTS

The National Radio Astronomy Observatory is a facility of the National Science Foundation operated under cooperative agreement by Associated Universities, Inc. Support for this work was provided by the NSF through the Grote Reber Fellowship Program administered by Associated Universities, Inc./National Radio Astronomy Observatory. This research was also supported by the NASA Ames Research Center via Cooperative Agreements NNA09DB30A, NNX15AD20A, and NNX16AF59G to J. O. Burns. D. Rapetti is supported by a NASA Postdoctoral Program Senior Fellowship at the NASA Ames Research Center, administered by the Universities Space Research Association under contract with NASA. This work was also directly supported by the NASA Solar System Exploration Virtual Institute cooperative agreement 80ARC017M0006. The authors gratefully acknowledge the Equinox Farm, LLC. for hosting and providing utilities for the CTP. B. Nhan would also like to thank K. Makhija for his comments on the instrumentation description.

## APPENDIX

### A. CONVERSION BETWEEN JONES AND MUELLER MATRICES

For a given dual polarization antenna, the antenna beam pattern can be described in terms of a  $2 \times 2$  Jones matrix, with the  $(\theta, \phi, \nu)$  notations suppressed for the ease of reading, as,

$$\mathbf{J}_{\text{ant}} = \begin{pmatrix} J_{11} & J_{12} \\ J_{21} & J_{22} \end{pmatrix} = \begin{pmatrix} |E_{\theta}^X| e^{i\Phi_{\theta}^X} & |E_{\phi}^X| e^{i\Phi_{\phi}^X} \\ |E_{\theta}^Y| e^{i\Phi_{\theta}^Y} & |E_{\phi}^Y| e^{i\Phi_{\phi}^Y} \end{pmatrix}, \quad (\text{A1})$$

where  $|E|$  and  $\Phi$  are the magnitude and phase of the  $\theta$  and  $\phi$  components of the farfield pattern. The output signal  $E$ -fields received by both polarization the antenna from the incoming  $E$ -fields is given by  $\mathbf{E}_{\text{out}} = \mathbf{J}_{\text{ant}} \mathbf{E}_{\text{in}}$  or in matrix form,

$$\begin{pmatrix} E_X \\ E_Y \end{pmatrix} = \begin{pmatrix} J_{11} & J_{12} \\ J_{21} & J_{22} \end{pmatrix} \begin{pmatrix} E_x \\ E_y \end{pmatrix}_{\text{in}}. \quad (\text{A2})$$

Subsequently, the coherency vectors for the output and input signal can be computed by taking the outer product of the  $E$ -fields and their complex conjugates as  $\mathbf{C} = \mathbf{E} \otimes \mathbf{E}^*$ , similar to Equation (B1), to produce the relation,

$$\mathbf{C}_{\text{out}} = (\mathbf{J}_{\text{ant}} \otimes \mathbf{J}_{\text{ant}}^*) \mathbf{C}_{\text{in}}. \quad (\text{A3})$$

Using the definition of the Stokes parameters as the linear combination of the autocorrelation and cross-correlation of the  $E$ -fields, the Stokes vector can be written in terms of the coherency vector as  $\mathbf{S} = \mathbf{A} \mathbf{C}$  for both the input and

output signal, where

$$\mathbf{A} = \begin{pmatrix} 1 & 0 & 0 & 1 \\ 1 & 0 & 0 & -1 \\ 0 & 1 & 1 & 0 \\ 0 & i & -i & 0 \end{pmatrix}, \quad (\text{A4})$$

to obtain the relation between the input and output Stokes vectors as,

$$\mathbf{S}_{\text{out}} = \mathbf{A}(\mathbf{J}_{\text{ant}} \otimes \mathbf{J}_{\text{ant}}^*)\mathbf{A}^{-1}\mathbf{S}_{\text{in}} = \mathbf{M}_{\text{ant}}\mathbf{S}_{\text{in}}, \quad (\text{A5})$$

where  $\mathbf{M}_{\text{ant}}$  is the  $4 \times 4$  antenna Mueller matrix. Therefore,

$$\mathbf{M}_{\text{ant}} = \mathbf{A}(\mathbf{J}_{\text{ant}} \otimes \mathbf{J}_{\text{ant}}^*)\mathbf{A}^{-1} \quad (\text{A6})$$

$$= \begin{pmatrix} 0.5(E_1 + E_2 + E_3 + E_4) & 0.5(E_1 - E_2 - E_3 + E_4) & F_{13} + F_{42} & -G_{13} - G_{42} \\ 0.5(E_1 - E_2 + E_3 - E_4) & 0.5(E_1 + E_2 - E_3 - E_4) & F_{13} - F_{42} & -G_{13} + G_{42} \\ F_{14} + F_{32} & F_{14} - F_{32} & F_{12} + F_{34} & -G_{12} + G_{34} \\ G_{14} + G_{32} & G_{14} - G_{32} & G_{12} + G_{34} & F_{12} - F_{34} \end{pmatrix}, \quad (\text{A7})$$

where

$$E_k = J_k J_k^*, \quad (\text{A8})$$

$$F_{kl} = F_{lk} = \text{Re}(J_k J_l^*) = \text{Re}(J_k^* J_l), \quad (\text{A9})$$

$$G_{kl} = -G_{lk} = \text{Im}(J_k J_l^*) = -\text{Im}(J_k^* J_l), \quad (\text{A10})$$

for  $k, l \in \{1, 2, 3, 4\}$ , and  $\{J_1, J_2, J_3, J_4\}$  respectively representing the four components  $\{J_{11}, J_{22}, J_{12}, J_{21}\}$  of the Jones matrix. A more detailed derivation of the conversion between Jones and Mueller matrices can commonly be found in literature, such as one provided in the Appendix 4 of Fujiwara (2007).

## B. CALIBRATION FOR STOKES ANTENNA TEMPERATURE

To derive the formulae to convert the correlation spectra into equivalent temperature units, we first note that the complex  $E$ -fields for each polarization in the coherency vector,

$$\mathbf{C}(t, \nu) = \begin{pmatrix} E_X E_X \\ E_X E_Y \\ E_Y E_X \\ E_Y E_Y \end{pmatrix}_{(t, \nu)}, \quad (\text{B1})$$

are equivalent to the complex antenna voltages,  $\tilde{V}_X(t, \nu)$  and  $\tilde{V}_Y(t, \nu)$ , which are acquired from Fourier transforming the sampled antenna voltages. Meanwhile, the power transducer gain  $G_T(t, \nu)$  is defined as the magnitude square of the complex voltage gain  $g_T(t, \nu)$ , i.e.,  $G_T = |g_T|^2$ . The noise power  $P_n(\nu, t)$  from the FE signal path can be written as the absolute square of the complex noise voltage  $\tilde{V}_n(t, \nu)$ , and  $P_n(t, \nu) = \langle |\tilde{V}_n \tilde{V}_n^*| \rangle = k_B \Delta \nu T_n(t, \nu)$  with the Boltzmann constant  $k_B$ . Hence the monochromatic  $E$ -fields of both polarizations can be parametrized as,

$$E_X(t, \nu) = \tilde{V}_X(t, \nu) = g_{T,X}(t, \nu) \left[ \tilde{V}_{\text{ant},X}(t, \nu) + \tilde{V}_{n,X}(t, \nu) \right], \quad (\text{B2})$$

$$E_Y(t, \nu) = \tilde{V}_Y(t, \nu) = g_{T,Y}(t, \nu) \left[ \tilde{V}_{\text{ant},Y}(t, \nu) + \tilde{V}_{n,Y}(t, \nu) \right], \quad (\text{B3})$$

where  $\tilde{V}_{\text{ant}}(t, \nu)$  is the antenna voltage signal of each polarization when observing the sky, where  $P_{\text{ant}}(t, \nu) = \langle |\tilde{V}_{\text{ant}} \tilde{V}_{\text{ant}}^*| \rangle = k_B \Delta \nu T_{\text{ant}}(t, \nu)$ . With these two equations, we can write the correlation terms in the coherency vector as,

$$\langle \tilde{V}_X \tilde{V}_X^* \rangle = G_{T,X} \left( \langle \tilde{V}_{\text{ant},X} \tilde{V}_{\text{ant},X}^* \rangle + \langle \tilde{V}_{n,X} \tilde{V}_{n,X}^* \rangle + \langle \tilde{V}_{\text{ant},X} \tilde{V}_{n,X}^* \rangle + \langle \tilde{V}_{\text{ant},X}^* \tilde{V}_{n,X} \rangle \right), \quad (\text{B4})$$

$$\langle \tilde{V}_Y \tilde{V}_Y^* \rangle = G_{T,Y} \left( \langle \tilde{V}_{\text{ant},Y} \tilde{V}_{\text{ant},Y}^* \rangle + \langle \tilde{V}_{n,Y} \tilde{V}_{n,Y}^* \rangle + \langle \tilde{V}_{\text{ant},Y} \tilde{V}_{n,Y}^* \rangle + \langle \tilde{V}_{\text{ant},Y}^* \tilde{V}_{n,Y} \rangle \right), \quad (\text{B5})$$

$$\langle \tilde{V}_X \tilde{V}_Y^* \rangle = \sqrt{G_{T,X} G_{T,Y}} \left( \langle \tilde{V}_{\text{ant},X} \tilde{V}_{\text{ant},Y}^* \rangle + \langle \tilde{V}_{n,X} \tilde{V}_{n,Y}^* \rangle + \langle \tilde{V}_{\text{ant},X} \tilde{V}_{n,Y}^* \rangle + \langle \tilde{V}_{\text{ant},Y} \tilde{V}_{n,X}^* \rangle \right), \quad (\text{B6})$$

$$\langle \tilde{V}_Y \tilde{V}_X^* \rangle = \sqrt{G_{T,X} G_{T,Y}} \left( \langle \tilde{V}_{\text{ant},X} \tilde{V}_{\text{ant},Y}^* \rangle + \langle \tilde{V}_{n,Y} \tilde{V}_{n,X}^* \rangle + \langle \tilde{V}_{\text{ant},Y} \tilde{V}_{n,X}^* \rangle + \langle \tilde{V}_{\text{ant},X} \tilde{V}_{n,Y} \rangle \right), \quad (\text{B7})$$

where the  $(t, \nu)$  notation has been suppressed for the ease of reading, and  $\langle \dots \rangle$  represents an ensemble average. The equivalent antenna temperatures resulting from these auto- and cross-powers can be written as

$$T_{\text{ant},kl}(t, \nu) = \frac{\langle \tilde{V}_{\text{ant},k} \tilde{V}_{\text{ant},l}^* \rangle}{k_B \Delta \nu}, \quad (\text{B8})$$

where the subscripts  $\{k, l\}$  correspond to the  $X$  or  $Y$  polarizations.



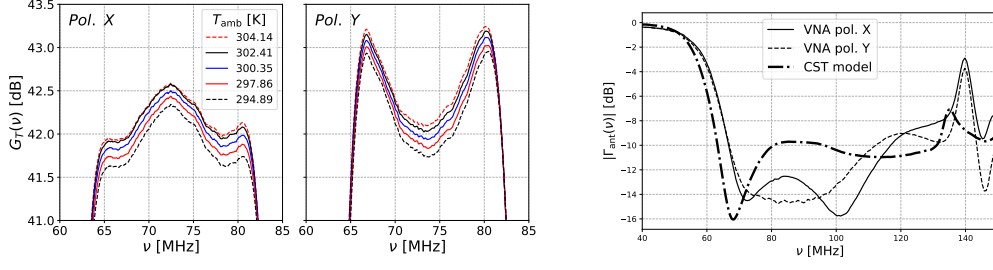


FIG. 22.— (Left) Laboratory measurement of the transducer gain of both polarizations as the operating temperature of the thermal enclosure is being varies. (Right) Antenna reflection coefficients measured as  $S_{11}$  for both polarized and compared to the CST model. The difference between the measurement and model is due to the frequency response of the passive balun which was not included in the CST model. Nonetheless, the actual calibration utilized the direct  $S_{11}$  measurement for each respective polarization, not the CST model.

Subsequently, the calibrated Stokes parameters, which were computed with the auto-spectra and cross-spectra, can be written in temperature unit as the following,

$$I_{\text{cal}}(t, \nu) = T_{\text{ant},XX}(t, \nu) + T_{\text{ant},YY}(t, \nu)$$

$$= \frac{1}{k_B \Delta \nu} \left[ \left( \frac{\langle \tilde{V}_X \tilde{V}_X^* \rangle}{G_{T,X}} + \frac{\langle \tilde{V}_Y \tilde{V}_Y^* \rangle}{G_{T,Y}} \right) - (T_{n,X} + T_{n,Y}) - 2\text{Re} \left( \langle \tilde{V}_{\text{ant},X} \tilde{V}_{n,X}^* \rangle \right) - 2\text{Re} \left( \langle \tilde{V}_{\text{ant},Y} \tilde{V}_{n,Y}^* \rangle \right) \right], \quad (\text{B9})$$

$$Q_{\text{cal}}(t, \nu) = T_{\text{ant},XX}(t, \nu) - T_{\text{ant},YY}(t, \nu)$$

$$= \frac{1}{k_B \Delta \nu} \left[ \left( \frac{\langle \tilde{V}_X \tilde{V}_X^* \rangle}{G_{T,X}} - \frac{\langle \tilde{V}_Y \tilde{V}_Y^* \rangle}{G_{T,Y}} \right) - (T_{n,X} - T_{n,Y}) - 2\text{Re} \left( \langle \tilde{V}_{\text{ant},X} \tilde{V}_{n,X}^* \rangle \right) + 2\text{Re} \left( \langle \tilde{V}_{\text{ant},Y} \tilde{V}_{n,Y}^* \rangle \right) \right], \quad (\text{B10})$$

$$U_{\text{cal}}(t, \nu) = T_{\text{ant},XY}(t, \nu) + T_{\text{ant},YX}(t, \nu)$$

$$= \frac{2}{k_B \Delta \nu} \left[ \frac{\text{Re} \left( \langle \tilde{V}_X \tilde{V}_Y^* \rangle \right)}{\sqrt{G_{T,X} G_{T,Y}}} - \text{Re} \left( \langle \tilde{V}_{n,X} \tilde{V}_{n,Y}^* \rangle \right) - \text{Re} \left( \langle \tilde{V}_{\text{ant},X} \tilde{V}_{n,Y}^* \rangle \right) - \text{Re} \left( \langle \tilde{V}_{\text{ant},Y} \tilde{V}_{n,X}^* \rangle \right) \right], \quad (\text{B11})$$

$$V_{\text{cal}}(t, \nu) = i \left[ T_{\text{ant},XY}(t, \nu) - T_{\text{ant},YX}(t, \nu) \right]$$

$$= \frac{-2}{k_B \Delta \nu} \left[ \frac{\text{Im} \left( \langle \tilde{V}_X \tilde{V}_Y^* \rangle \right)}{\sqrt{G_{T,X} G_{T,Y}}} - \text{Im} \left( \langle \tilde{V}_{n,X} \tilde{V}_{n,Y}^* \rangle \right) - \text{Im} \left( \langle \tilde{V}_{\text{ant},X} \tilde{V}_{n,Y}^* \rangle \right) - \text{Im} \left( \langle \tilde{V}_{\text{ant},Y} \tilde{V}_{n,X}^* \rangle \right) \right], \quad (\text{B12})$$

Since the sky signal ( $\tilde{V}_{\text{ant}}$ ) and the electronic noise ( $\tilde{V}_n$ ) are uncorrelated both within the same polarization and among the two polarizations, time averaged values of the cross terms cancel out. Hence, the calibrated Stokes parameters reduce to Equations (13)-(16).

### C. SUPPLEMENTARY CTP MEASUREMENTS

#### Calibration Data

The CTP calibration equations are based on laboratory measurement of the system's FE and receiver. Since the entire signal chain, from the FE' input to the output at the coaxial cables before entering the ADC, is considered as a single two-port network, two separate sets of  $S$ - and noise-parameters were determined for both polarizations. Additional details of the measurements and related information can be found in Nhan (2018).

The  $S$ -parameters were measured with a VNA connector to the input and output of the CTP's system at different set operating temperature ( $T_{\text{amb}} \sim 20 - 35^\circ\text{C}$ ). Then they are least-squares fitted for a set of coefficients as functions of frequency and  $T_{\text{amb}}$ . The corresponding transducer gain  $G_T(\nu, T_{\text{amb}})$  were calculated with Equation (17), using  $\Gamma_{\text{src}} = 50 \Omega$  in the laboratory (Figure 22, left), and  $\Gamma_{\text{src}} = \Gamma_{\text{ant}}(\nu)$  (Figure 22, right) for the CTP sleeved dipole in the field).

The CTP's noise parameters were determined by simultaneously fit the measured  $T_n(\nu, Z_{\text{src}})$  of the five reference input fixtures to Equation (18) (Figure 23, left), where the noise factor  $NF(\nu) = 10 \log_{10} F_n(\nu) = 10 \log_{10} [1 + T_n(\nu)/T_0]$ . However, since  $T_{\text{min}}(\nu)$  in that equation is a free constant, the MCMC fit does not converge unless an initial estimate of the  $T_{\text{min}}(\nu)$  is provided. For the CTP frontend, by assuming  $T_n(\nu)$  is dominated by the first stage LNA according to Friis's formula,  $T_{\text{min}}(\nu)$  was constrained by a detailed circuit model of the LNA using the ADS (Keysight's Advanced Design Simulation) program. Subsequently, the remaining three noise parameters were determined by the MCMC fit.

The MCMC fit of  $\{ \text{Re}[\Gamma_{\text{opt}}(\nu)], \text{Im}[\Gamma_{\text{opt}}(\nu)], N(\nu) \}$  are presented in the right panel of Figure 23, where  $F_{\text{min}}(\nu) = 1 + T_{\text{min}}(\nu)/T_0$  is the noise factor, and  $r_n(\nu) = R_n(\nu)/Z_0$  is the normalized equivalent noise resistance with the relation between  $N(\nu)$  and  $R_n(\nu)$  defined in (18).

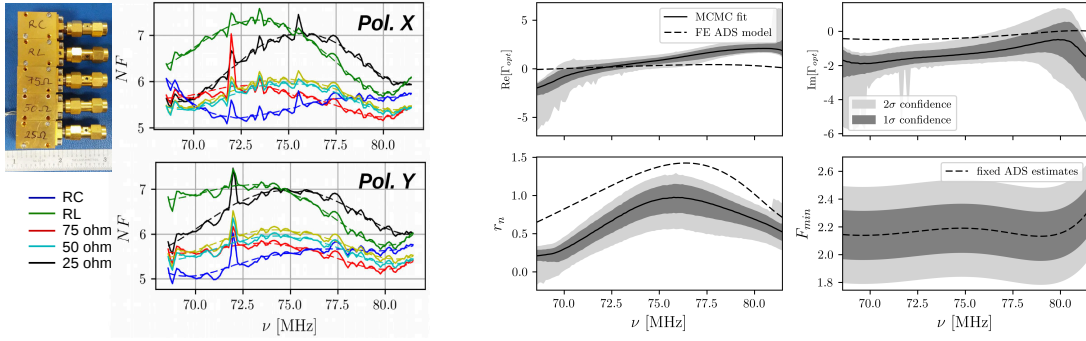


FIG. 23.— (a) Noise figures for polarization X (upper panel) and Y (lower panel) of the CTP system (except the sleeved antenna) measured for different input impedance modules, including 25 $\Omega$ , 50 $\Omega$ , 75 $\Omega$ , *RC*, and *RL* loads (solid). The best fit values of these  $NF$  are superimposed (dashed). (b) MCMC fit of the noise parameters based on the lab measured  $F_n(\nu)$  and  $\Gamma_{\text{src}}(\nu)$ , along with the ADS estimation of  $F_{\text{min}}(\nu)$  for the FE RF module. Since  $F_{\text{min}}(\nu)$  is a free constant, the MCMC fit does not converge unless it is constrained.

### Effects of SavitzkyGolay Filter's Window Size

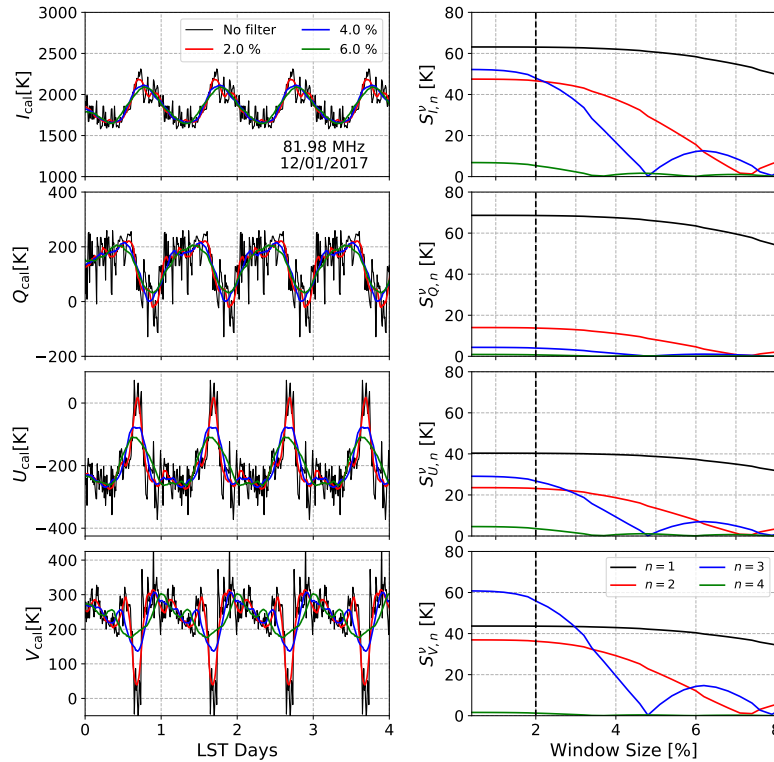


FIG. 24.— Effects of SavitzkyGolay filter window size on the recovered magnitude of the harmonic components in the induced Stokes parameters. The filter computes the moving average of the Stokes parameters to suppress the high frequency noise. As a result, the larger the window size is, the more high-order harmonics are filtered out. (Left) The Stokes parameters of different window sizes: 2%, 4%, 6% of the total data length compared with no filtering. (Right) Magnitudes of  $n = 1, 2, 3, 4$  components decrease once the window size gets too large. The window size (in percentage relative to the data length) is chosen to be around 2% of the total data length so that low-order harmonics of interest are preserved (dashed line).

### REFERENCES

- Barkana, R. 2016, *Phys. Rep.*, 645, 1, doi: 10.1016/j.physrep.2016.06.006
- Bernardi, G., McQuinn, M., & Greenhill, L. J. 2015, *ApJ*, 799, 90, doi: 10.1088/0004-637X/799/1/90
- Bernardi, G., de Bruyn, A. G., Brentjens, M. A., et al. 2009, *A&A*, 500, 965, doi: 10.1051/0004-6361/200911627
- Bernardi, G., de Bruyn, A. G., Harker, G., et al. 2010, *A&A*, 522, A67, doi: 10.1051/0004-6361/200913420
- Bittner, J. M., & Loeb, A. 2011, *Journal of Cosmology and Astroparticle Physics*, 4, 38, doi: 10.1088/1475-7516/2011/04/038
- Bowman, J. D., & Rogers, A. E. E. 2010, *Nature*, 468, 796, doi: 10.1038/nature09601
- Bowman, J. D., Rogers, A. E. E., & Hewitt, J. N. 2008, *ApJ*, 676, 1, doi: 10.1086/528675
- Bowman, J. D., Rogers, A. E. E., Monsalve, R. A., Mozdzen, T. J., & Mahesh, N. 2018, *Nature*, 555, 67 EP

- Bowman, J. D., Cairns, I., Kaplan, D. L., et al. 2013, *PASA*, 30, e031, doi: 10.1017/pas.2013.009
- Bradley, R. F., Tauscher, K., Rapetti, D., & Burns, J. O. 2019, *ApJ*, 874, 153, doi: 10.3847/1538-4357/ab0d8b
- Burns, J. O., Lazio, J., Bale, S., et al. 2012, *Advances in Space Research*, 49, 433, doi: 10.1016/j.asr.2011.10.014
- Burns, J. O., Bradley, R., Tauscher, K., et al. 2017, *ApJ*, 844, 33, doi: 10.3847/1538-4357/aa77f4
- Collin, R. E. 2007, *Foundations for Microwave Engineering* (John Wiley & Sons)
- Datta, A., Bradley, R., Burns, J. O., et al. 2016, *ApJ*, 831, 6, doi: 10.3847/0004-637X/831/1/6
- de Oliveira-Costa, A., Tegmark, M., Gaensler, B. M., et al. 2008, *MNRAS*, 388, 247, doi: 10.1111/j.1365-2966.2008.13376.x
- DeBoer, D. R., Parsons, A. R., Aguirre, J. E., et al. 2017, *Publications of the Astronomical Society of the Pacific*, 129, 045001, doi: 10.1088/1538-3873/129/974/045001
- Dicke, R. H. 1982, 1946, *The Measurement of Thermal Radiation at Microwave Frequencies*, ed. W. T. Sullivan, III, 106
- Engberg, J., & Larsen, T. 1995, *Noise Theory of Linear and Nonlinear Circuits* (John Wiley & Sons)
- Falcke, H., Klein Wolt, M., Ping, J., & Chen, L. 2018, in *American Astronomical Society Meeting Abstracts #232*, Vol. 232, 211.03
- Frigo, M., & Johnson, S. G. 2005, in *PROCEEDINGS OF THE IEEE*, 216–231
- Fujiwara, H. 2007, *Spectroscopic ellipsometry: principles and applications* (John Wiley & Sons)
- Furlanetto, S. R. 2006, *MNRAS*, 371, 867, doi: 10.1111/j.1365-2966.2006.10725.x
- Furlanetto, S. R., Oh, S. P., & Briggs, F. H. 2006, *Phys. Rep.*, 433, 181, doi: 10.1016/j.physrep.2006.08.002
- Gehlot, B. K., Mertens, F. G., Koopmans, L. V. E., et al. 2018, *arXiv e-prints*, arXiv:1809.06661, <https://arxiv.org/abs/1809.06661>
- Greenhill, L. J., & LEDA Collaboration. 2015, in *American Astronomical Society Meeting Abstracts*, Vol. 225, *American Astronomical Society Meeting Abstracts #225*, 403.07
- Guzmán, A. E., May, J., Alvarez, H., & Maeda, K. 2011, *A&A*, 525, A138, doi: 10.1051/0004-6361/200913628
- Harker, G. J. A., Pritchard, J. R., Burns, J. O., & Bowman, J. D. 2012, *MNRAS*, 419, 1070, doi: 10.1111/j.1365-2966.2011.19766.x
- Haslam, C. G. T., Salter, C. J., Stoffel, H., & Wilson, W. E. 1982, *A&AS*, 47, 1
- Heinzel, G., Rüdiger, A., & Schilling, R. 2002, *Spectrum and spectral density estimation by the Discrete Fourier transform (DFT)*, including a comprehensive list of window functions and some new at-top windows, *Tech. rep.*, Max Planck Institute for Gravitational Physics
- Hills, R., Kulkarni, G., Meerburg, P. D., & Puchwein, E. 2018, *ArXiv e-prints*, arXiv:1805.01421, <https://arxiv.org/abs/1805.01421>
- Jelić, V., Zaroubi, S., Labropoulos, P., et al. 2010, *MNRAS*, 409, 1647, doi: 10.1111/j.1365-2966.2010.17407.x
- Kogut, A. 2012, *ApJ*, 753, 110, doi: 10.1088/0004-637X/753/2/110
- Kraus, J. D. 1986, *Radio Astronomy* (2nd ed.; Powell, OH: Cygnus-Quasar Books)
- Liu, A., Pritchard, J. R., Tegmark, M., & Loeb, A. 2013, *Phys. Rev. D*, 87, 043002, doi: 10.1103/PhysRevD.87.043002
- Mellema, G., Koopmans, L. V. E., Abdalla, F. A., et al. 2013, *Experimental Astronomy*, 36, 235, doi: 10.1007/s10686-013-9334-5
- Mirocha, J. 2014, *MNRAS*, 443, 1211, doi: 10.1093/mnras/stu1193
- Mirocha, J., Furlanetto, S. R., & Sun, G. 2017, *MNRAS*, 464, 1365, doi: 10.1093/mnras/stw2412
- Mirocha, J., Harker, G. J. A., & Burns, J. O. 2013, *ApJ*, 777, 118, doi: 10.1088/0004-637X/777/2/118
- , 2015, *ApJ*, 813, 11, doi: 10.1088/0004-637X/813/1/11
- Monsalve, R. A., Rogers, A. E. E., Bowman, J. D., & Mozdzien, T. J. 2017, *ApJ*, 835, 49, doi: 10.3847/1538-4357/835/1/49
- Mozdzien, T. J., Bowman, J. D., Monsalve, R. A., & Rogers, A. E. E. 2016, *MNRAS*, 455, 3890, doi: 10.1093/mnras/stv2601
- Nhan, B. D. 2018, PhD thesis, University of Colorado at Boulder
- Nhan, B. D., Bradley, R. F., & Burns, J. O. 2017, *ApJ*, 836, 90, doi: 10.3847/1538-4357/836/1/90
- Paciga, G., Albert, J. G., Bandura, K., et al. 2013, *MNRAS*, 433, 639, doi: 10.1093/mnras/stt753
- Parsons, A. R., Backer, D. C., Foster, G. S., et al. 2010, *AJ*, 139, 1468, doi: 10.1088/0004-6256/139/4/1468
- Patra, N., Subrahmanyan, R., Raghunathan, A., & Udaya Shankar, N. 2013, *Experimental Astronomy*, 36, 319, doi: 10.1007/s10686-013-9336-3
- Petrovic, N., & Oh, S. P. 2011, *MNRAS*, 413, 2103, doi: 10.1111/j.1365-2966.2011.18276.x
- Philip, L., Abdurashidova, Z., Chiang, H. C., et al. 2019, *Journal of Astronomical Instrumentation*, 8, 1950004, doi: 10.1142/S2251171719500041
- Piepmeyer, J. R., Long, D. G., & Njoku, E. G. 2008, *IEEE Transactions on Geoscience and Remote Sensing*, 46, 516, doi: 10.1109/TGRS.2007.909597
- Price, D. C., Greenhill, L. J., Fialkov, A., et al. 2018, *MNRAS*, 478, 4193, doi: 10.1093/mnras/sty1244
- Pritchard, J. R., & Loeb, A. 2010, *Phys. Rev. D*, 82, 023006, doi: 10.1103/PhysRevD.82.023006
- , 2012, *Reports on Progress in Physics*, 75, 086901, doi: 10.1088/0034-4885/75/8/086901
- Rogers, A. E. E., & Bowman, J. D. 2012, *Radio Science*, 47, RS0K06, doi: 10.1029/2011RS004962
- Sathyanarayana Rao, M., Subrahmanyan, R., Udaya Shankar, N., & Chluba, J. 2017a, *ApJ*, 840, 33, doi: 10.3847/1538-4357/aa69bd
- , 2017b, *AJ*, 153, 26, doi: 10.3847/1538-3881/153/1/26
- Sauer, H. H., & Wilkinson, D. C. 2008, *Space Weather*, 6
- Shaver, P. A., Windhorst, R. A., Madau, P., & de Bruyn, A. G. 1999, *A&A*, 345, 380
- Singh, S., Subrahmanyan, R., Udaya Shankar, N., et al. 2017, *ApJ*, 845, L12, doi: 10.3847/2041-8213/aa831b
- Sokolowski, M., Tremblay, S. E., Wayth, R. B., et al. 2015a, *PASA*, 32, e004, doi: 10.1017/pasa.2015.3
- Sokolowski, M., Wayth, R. B., Tremblay, S. E., et al. 2015b, *ApJ*, 813, 18, doi: 10.1088/0004-637X/813/1/18
- Sukumar, S. 1987, *Journal of Astrophysics and Astronomy*, 8, 281, doi: 10.1007/BF02714893
- Sutinjo, A., O’Sullivan, J., Lenc, E., et al. 2015, *Radio Science*, 50, 52, doi: 10.1002/2014RS005517
- Tauscher, K., Rapetti, D., & Burns, J. O. 2018a, *Journal of Cosmology and Astro-Particle Physics*, 2018, 015, doi: 10.1088/1475-7516/2018/12/015
- Tauscher, K., Rapetti, D., Burns, J. O., & Switzer, E. 2018b, *ApJ*, 853, 187, doi: 10.3847/1538-4357/aaa41f
- Tegmark, M., Eisenstein, D. J., Hu, W., & de Oliveira-Costa, A. 2000, *ApJ*, 530, 133, doi: 10.1086/308348
- Testori, J. C., Reich, P., & Reich, W. 2008, *A&A*, 484, 733, doi: 10.1051/0004-6361:20078842
- Tingay, S. J., Goeke, R., Bowman, J. D., et al. 2013, *PASA*, 30, e007, doi: 10.1017/pasa.2012.007
- Tripe, S. 2014, *Journal of Korean Astronomical Society*, 47, 15, doi: 10.5303/JKAS.2014.47.1.015
- van Bemmell, I. 2007, in *From Planets to Dark Energy: the Modern Radio Universe*, 12
- van Haarlem, M. P., Wise, M. W., Gunst, A. W., et al. 2013, *A&A*, 556, A2, doi: 10.1051/0004-6361/201220873
- Vedantham, H. K., Koopmans, L. V. E., de Bruyn, A. G., et al. 2014, *MNRAS*, 437, 1056, doi: 10.1093/mnras/stt1878
- Voytek, T. C., Natarajan, A., Jáuregui García, J. M., Peterson, J. B., & López-Cruz, O. 2014, *ApJ*, 782, L9, doi: 10.1088/2041-8205/782/1/L9
- Waelkens, A., Jaffe, T., Reinecke, M., Kitaura, F. S., & Enßlin, T. A. 2009, *A&A*, 495, 697, doi: 10.1051/0004-6361:200810564
- Wilson, T. L., Rohlf, K., & Hüttemeister, S. 2009, *Tools of Radio Astronomy* (5th ed; Berlin, Germany: Springer-Verlag)
- Wolleben, M., Landecker, T. L., Reich, W., & Wielebinski, R. 2006, *A&A*, 448, 411, doi: 10.1051/0004-6361:20053851